iScience

CellPress
OPEN ACCESS

Article

Tumor-derived covalent organic framework nanozymes for targeted chemo-phototherapy combination therapy

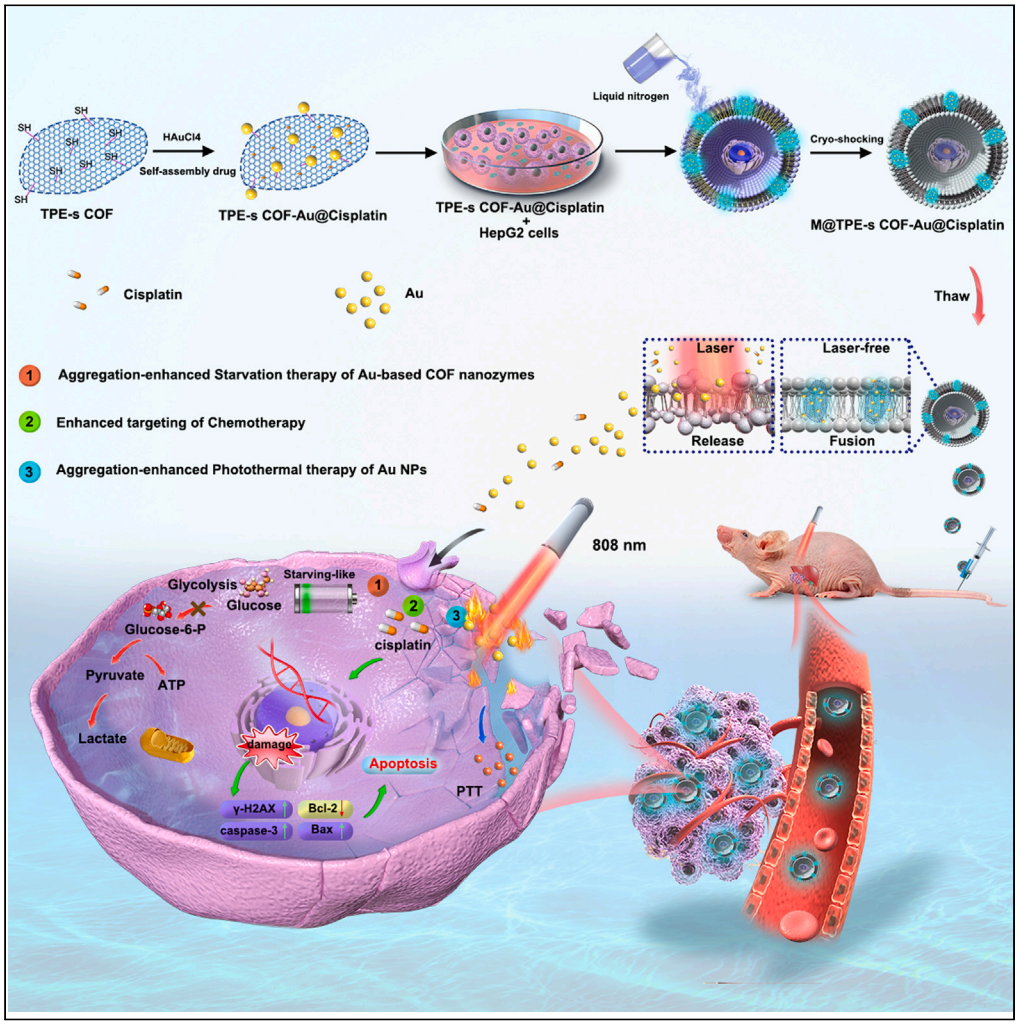

Shengnan Zhou, Tian Tian, Tao Meng, ..., Jialu Zhuang, Hua Wang, Guiyang Zhang

wanghua@ahmu.edu.cn (H.W.)
guiyangzhang@ahmu.edu.cn (G.Z.)

Highlights

An AIEgen-based COF nanozyme is developed in this work

NIR could significantly promote the catalytic-mimicking activity of TPE-s COF-Au

Tumor-derived COF nanozyme exhibited efficient anti-tumor capacity *in vitro* and *in vivo*

Zhou et al., iScience *26*, 107348
August 18, 2023
https://doi.org/10.1016/j.isci.2023.107348

iScience

CellPress
OPEN ACCESS

Article

Tumor-derived covalent organic framework nanozymes for targeted chemo-photothermal combination therapy

Shengnan Zhou,[1,4] Tian Tian,[2,4] Tao Meng,[1] Jin Wu,[1] Danyou Hu,[1] Qiaobo Liao,[3] Jialu Zhuang,[2] Hua Wang,[2,*] and Guiyang Zhang[1,5,*]

SUMMARY

Covalent organic frameworks (COFs) have garnered enormous attention in anti-cancer therapy recently. However, the intrinsic drawbacks such as poor biocompatibility and low target-specificity greatly restrain the full clinical implementation of COF. Herein, we report a biomimetic multifunctional COF nanozyme, which consists of AIEgen-based COF (TPE-s COF) with encapsulated gold nanoparticles (Au NPs). The nanozyme was co-cultured with HepG2 cells until the cell membrane was fused with lipophilic TPE-s COF-Au@Cisplatin. By using the cryo-shocking method, we fabricated an inactivated form of the TPE-s COF-Au@Cisplatin nanozyme endocytosed in the HepG2 cell membrane (M@TPE-s COF-Au@Cisplatin), which lost their proliferative ability and pathogenicity. Upon laser irradiation, the M@TPE-s COF-Au@Cisplatin nanozymes cleaved, thereby releasing the TPE-s COF-Au nanozyme and Cisplatin to exert their photothermal and drug therapeutic effect. This work opens a new avenue to the synthesis of tumor-derived fluorescent TPE-s COF-Au nanozymes for highly efficient, synergetic, and targeted chemo-photothermal combination therapy of liver cancer.

INTRODUCTION

Nano-biotechnology has revolutionized the field of drug delivery by developing nanocomposite systems as carriers. These systems have been combined with various tumor treatment strategies, attracting significant attention in biomedicine. In particular, multifunctional nanoparticle-anchored cell platforms have proven effective in delivering drugs to targeted cells, including engineered immune cells, stem cells, red blood cells, platelets, adipocytes, bacteria, and even inactivated cancer cells.[1–3] For instance, Gu et al. used the treated non-pathogenic acute myeloid leukemia (AML) dead cells to construct a drug delivery system with bone-marrow targeting function to improve the enrichment of doxorubicin in bone marrow, which inhibited the growth of AML cells.[4] Zhao et al. developed triple-negative breast cancer (TNBC) cells (Cell-αPD-1/Liposome) by conjugating anti-PD-1 (programmed death protein 1 inhibitor) and doxorubicin (DOX) liposomes to cell corpses, which can achieve chemoimmunotherapy against lung metastases.[5] These studies underscore the opportunity to leverage the intrinsic properties of tumor cell cadavers as powerful vehicles for targeted drug delivery. Autologous cancer-cell cadavers have several unique advantages as a drug delivery system. One key advantage is that they preserve the natural tendency of tumor cells to target the lesion site, which can improve the efficacy of the therapy. Additionally, the presence of tumor antigens in the cancer-cell cadavers can elicit an individualized immune response, potentially enhancing the overall therapeutic effect.[6–11] Therefore, it is worthwhile to explore the feasibility of using autologous tumor-cell-anchored multifunctional nanoparticles as novel therapeutic platforms for drug delivery to targets of interest.

On the other hand, chemotherapy and various local thermal-ablation techniques have been developed for treating unresectable orthotopic hepatocellular carcinoma (HCC). Of many techniques, percutaneous photothermal ablation is the main treatment for patients with small HCC. It is of prime importance to combine photothermal therapy and chemotherapy for patients who are not suitable for surgical resection or transplantation.[12] To this end, covalent organic frameworks (COFs), a novel class of pre-designable porous

[1]Department of Pharmacology, School of Basic Medical Sciences, Anhui Medical University, Hefei 230032, P.R. China

[2]Department of Oncology, the First Affiliated Hospital of Anhui Medical University, Hefei 230032, China

[3]School of Chemistry and Chemical Engineering, Nanjing University, Jiangsu 210023, China

[4]These authors contributed equally

[5]Lead contact

*Correspondence: wanghua@ahmu.edu.cn (H.W.), guiyangzhang@ahmu.edu.cn (G.Z.)

https://doi.org/10.1016/j.isci.2023.107348

polymers with regular network structures and amenable functionalities, have emerged as intriguing drug carriers for combined chemo and photothermal therapy. For instance, in 2018, Jia et al. developed a series of water-dispersible polymer-COF nanocomposites (PEG-CCM@APTES-COF-1) for *in vivo* drug delivery, exhibiting high stability, biodegradability, high drug loading capacity, and enhanced drug accumulation in tumors.[13] Chen et al. exfoliated a porphyrin COF (TP-Por COF) in the presence of cyanine (IR783) by ultrasonic exfoliation to afford IR783-loaded COF nanosheets (COF@IR783). Furthermore, they encapsulated anticancer prodrug, *cis*-aconitic anhydride-modified doxorubicin into the COF@IR783 to form a chemo-photothermal combination therapy system, which resulted in efficient tumor ablation.[14] The remarkable strides uncover the vast potential of COF in nano-drug carriers and photothermal therapy. However, the poor biocompatibility and low targeting present substantial obstacles to the biomedical applications of COF.[15–18] To circumvent these shortcomings, we envision that anchoring COF with unique invisible cell armors can endow COF carriers with good biocompatibility and specific targeting effect. Therefore, the development of autologous tumor-cell-anchored COF vectors is an exciting area of research in cancer therapy and holds the potential to provide new and effective treatment options for patients.

Nanozymes represent an emerging paradigm of nanomaterials that mimic the functions of natural enzymes. Recently, developing nanozymes as novel therapeutic catalytic nanoreactors offer an attractive clinical alternative for tumor treatment.[19–21] Compared to natural enzymes that suffer from inherent drawbacks, nanozymes are generally designable, cost-effective, and more stable.[22] In the quest for advanced nanozymes for tumor therapy, Au NPs offer a potent option since they are proven effective catalysts for the oxidation of β-D-glucose to gluconic acid. Glucose is the most abundant nutrient in the tumor microenvironment and malignant cells are prone to catabolizing glucose to obtain energy. Rossi et al. first reported that ''naked'' Au NPs could catalytically oxidize glucose while other metal nanomaterials did not exhibit significant catalytic-mimicking activities.[23] To mimic the glucose oxidase, Wu et al. encapsulated platinum NPs and Au NPs inside porphyrin metal-organic frameworks to fabricate a biomimetic nanoreactor for high therapeutic efficacy against cancer.[24] Such extraordinary activity for glucose oxidation reactions suggested that Au NPs could serve as a mimic for glucose oxidase. Nevertheless, long-term glucose starvation can cause toxic side effects on normal cells, such as immune cells and stem cells, which can also through glycolysis limit therapeutic effect.[25] As such, it is much desired to impart specific tumor-targeting abilities to Au NPs.

Herein, we report an aggregation-induced emission (AIEgen)-based COF (TPE-s COF) nanozyme featuring autologous tumor cell-specific fusion for dual-modal imaging and efficient chemo-photothermal combination therapy. The pendent thiol groups on the TPE-s COF stabilize glucose oxidase-mimicking Au NPs that possess photothermal properties. Moreover, the Au NPs could catalyze glucose into gluconic acid and H_2O_2, which lead to a restricted adenosine triphosphate (ATP) supply and influence the metabolism processes of tumor cells. Subsequently, cisplatin drugs were encapsulated inside the TPE-s COF-Au to form a lipophilic fluorescent TPE-s COF-Au@Cisplatin nanozyme. Afterward, the nanozyme was co-cultured with HepG2 cells until the HepG2 cell fused with lipophilic TPE-s COF-Au@Cisplatin. By a cryo-shocking method, a fusion of TPE-s COF-Au@Cisplatin nanozyme endocytosed in the HepG2 cell was generated (denoted as M@TPE-s COF-Au@Cisplatin). HepG2 cells maintained their structural integrity after being cryo-shocked but lost proliferation ability and pathogenicity. Besides, the integration of the AIE-active tetraphenyl ethylene unit into COF skeleton produced highly emissive TPE-s COF-Au, allowing for the *in vivo* imaging of the targeted release and metabolic process of AIEgen-based COF. Furthermore, upon the irradiation of laser light, the tumor cells ruptured, and synchronically released the fused TPE-s COF-Au nanozyme and Cisplatin to exert their therapeutic effect. This work, collectively validated by three animal models, provides a facile method for the synthesis of lipophilic, emissive TPE-s COF-Au nanozymes with autologous tumor cell-specific fusion for dual imaging and combination therapy.

RESULTS

Synthesis and characterization of M@TPE-s COF-Au@Cisplatin nanozyme

The synthesis of emissive COF carriers with high crystallinity, porosity, and stability is crucial for this work.[16,18] Hence, we synthesized an AIEgen-based COF (termed TPE-s COF) bearing tetraphenylethylene (TPE) moieties and pedant sulfhydryl groups by condensing 4,4′,4′,4″,4‴-(ethylene-1,1,2,2-tetraphenyl) tetrabenzaldehyde with 3,3′-dithiol-4,4′-diamino-biphenyl in a mixture of dioxane/mesitylene (*v*/*v* = 1/1) at 120°C for 3 days in a 45% isolated yield. Subsequently, $HAuCl_4$ was mixed with COF aqueous solution and $NaBH_4$ was added dropwise until the red color deepened. The strong Au-SH interaction readily

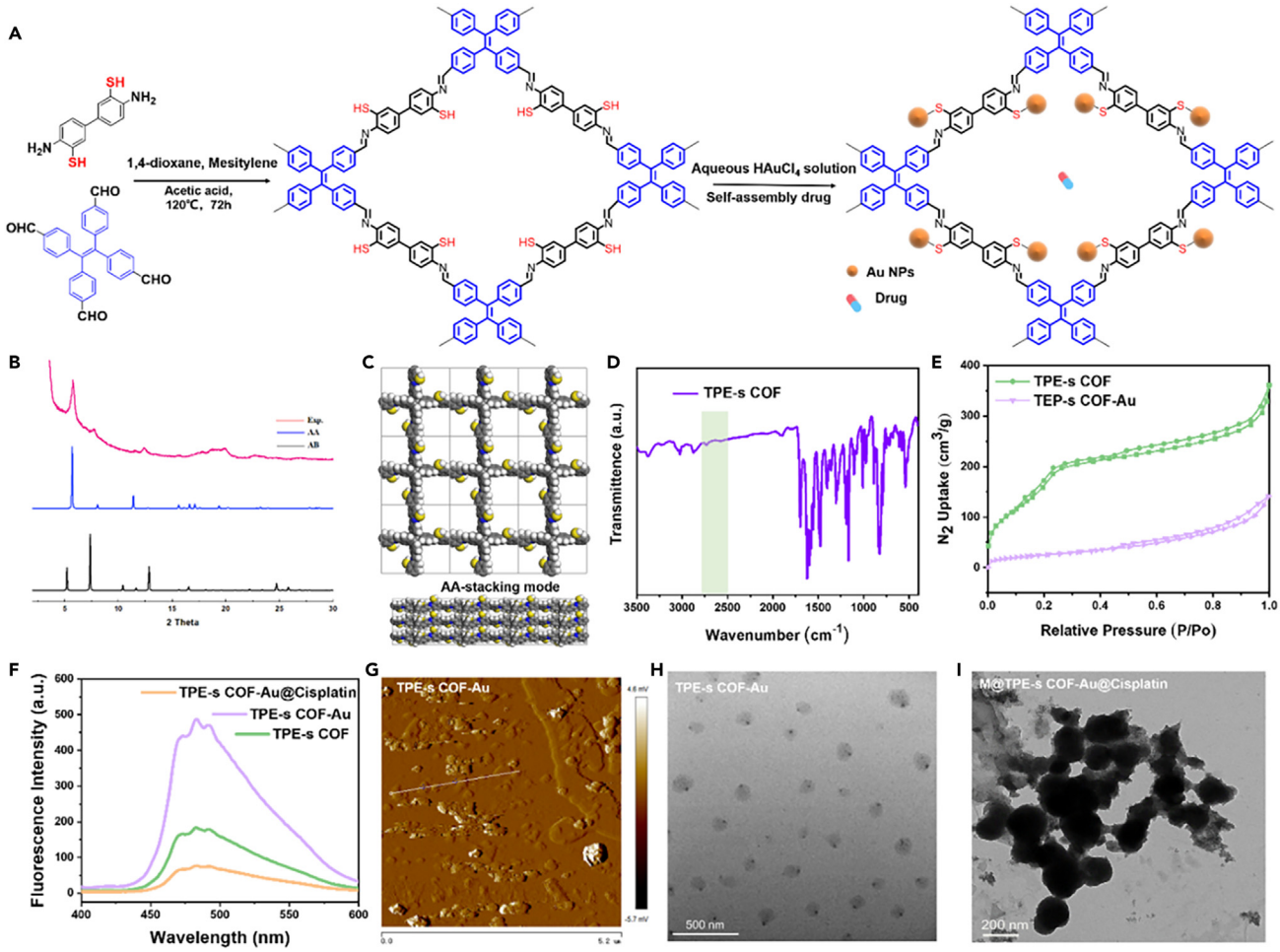

Figure 1. Synthesis schematic and characterization of TPE-s COF-Au@Cisplatin carriers

(A) Schematic illustration of the synthesis of TPE-s COF-Au@ Cisplatin carriers.

(B) PXRD patterns of TPE-s COF (experimentally observed (red), calculated AA-stacking mode of single-pore rhombic structure (blue), AB-stacking mode of single-pore Kagome structure (black).

(C) Crystal structure of the single-pore rhombic TPE-s COF in) AA stacking mode.

(D) FT-IR spectrum of the TPE-s COF.

(E) N_2 adsorption-desorption isotherms of TPE-s COF (green) and TPE-s COF-Au (purple).

(F) Fluorescence spectrum of TPE-s COF (green), TPE-s COF-Au (purple), and TPE-s COF-Au@Cisplatin (orange).

(G) AFM image of TPE-s COF-Au.

(H) TEM image of TPE-s COF-Au (Scale bar, 500 nm).

(I) TEM image of TPE-s COF-Au@Cisplatin carriers after encapsulating the HepG2 shock cell (Scale bar, 200 nm).

stabilizes Au NPs (Figure 1A), underpinning the robust and good photothermal properties.[26–29] The crystalline structure of TPE-s COF was determined by powder X-ray diffraction (PXRD) measurement in conjugation with computational simulation. The PXRD pattern of TPE-s COF exhibited an intense peak at 5.2°, which matched well with the simulated pattern (Figure 1B, red curve). Pawley refinement deduced a PXRD pattern (blue curve) consistent with the experimentally observed one. Theoretical simulations showed that the eclipsed AA stacking pattern of the rhombic lattice reproduced the peak positions and intensities of the PXRD pattern, while the AB stacking pattern (black curve) did not match well with the experimentally observed one. Thus, TPE-s COF adopts single-hole rhombic lattices with tetragonal micropores (Figures 1C and S1). The ^{13}C cross-polarization magic-angle spinning (CP-MAS) NMR spectrum of TPE-s COF revealed a resonance signal at 38.8 ppm, which is characteristic of C-S carbons (Figure S2).[30,31] Furthermore, the FT-IR spectrum of TPE-s COF showed a stretching band at 2522 cm^{-1} arising from thiol groups (Figure 1D), which were central to the binding with Au NP in subsequent steps.

To evaluate the porosity of TPE-s COF-Au, nitrogen adsorption-desorption analysis was conducted at 77 K. The Brunauer–Emmett–Teller surface area of TPE-s COF-Au (133 $m^2 g^{-1}$) is much lower than that of pristine TPE-s COF (638 $m^2 g^{-1}$) (Figure 1E). The pore size distribution of TPE-s COF-Au is significantly reduced relative to that of TPE-s COF (Figure S3). Additionally, TPE-s COF-Au emits more intense photoluminescence (PL) (Figure 1F) than that of pristine TPE-s COF, while the PL intensity of TPE-s COF-Au@ Cisplatin is weaker than that of pristine TPE-s COF. We surmise that Au NPs in TPE-s COF induces an aggregation enhancement effect, while the cisplatin fills the TPE-s COF pores and alleviates the enhancement effect.[32] Moreover, UV-vis absorption spectroscopy verified the enhancement effect of Au NPs (Figure S4).

Next, atomic force microscopy (AFM) images of TPE-s COF-Au (Figure 1G) exhibited rough surfaces and uneven transverse dimensions, approximately 100 nm in diameter and 10 nm in thickness. Transmission electron microscopy (TEM) showed TPE-s COF-Au carriers had a regular flake structure with a monodispersed size of ~100 nm (Figure 1H). It is worth noting that Au NPs are uniformly distributed on TPE-s COF with an average size of 8 nm. Upon the coating and cell co-cultivation with the HepG2, TPE-s COF-Au shows an increased size of ~230 nm whereas the size of the cell remains unchanged (Figure 1I).

Location and characterization of liquid nitrogen–treated M@TPE-s COF-Au@Cisplatin nanozyme

As schematically depicted in Figure 2A, the TPE-s COF-Au@ Cisplatin carrier was co-cultured with HepG2 cells that were cryo-shocked to afford cell membrane (M) fusion TPE-s COF nanoenzyme (termed M@TPE-s COF-Au@Cisplatin). The average hydrodynamic diameters of TPE-s COF-Au and M@TPE-s COF-Au@Cisplatin are ~100 nm and ~220 nm, respectively (Figures S5 and S6). In addition, the Zeta potential of TPE-s COF, TPE-s COF-Au@Cisplatin, and M@TPE-s COF-Au@ Cisplatin gradually decreased, indicating the increased negative charges (Figure 2B). Among them, the charge of the TPE-s COF is ~ -4 mV while that of TPE-s COF-Au@Cisplatin decreased to ~ -19 mV, mainly due to the reduction of chloroauric acid to Au NPs.[33,34] The charge of M@TPE-s COF-Au@Cisplatin decreased to ~ −28 mV due to the anionic HepG2 shock cell membrane surface.[35–37] These results collectively indicate that the surface properties of TPE-s COF-Au@Cisplatin carriers were improved after the encapsulation of the HepG2 shock cell.

We further demonstrated that lipophilic TPE-s COF-Au@Cisplatin was fused with the HepG2 cell. With the density of HepG2 cells from 1×10^6 to 1×10^7/mL, TPE-s COF-Au@Cisplatin carrier was added in and co-cultured for 6 h. After centrifugation and resuspension, the cells were placed into the uncontrolled-rate cell freezing medium, which was then immersed in liquid nitrogen for 12 h, thawed at 37°C, and finally collected via centrifugation. The tetramethyl azozo blue (MTT) assay showed that live cells exhibited proliferative activity while shock cells did not (Figure 2C). In addition, the Zeta potential of the live cell was measured to be ~ −23 mV, while the shock cell almost had no Zeta potential (Figure 2D). Furthermore, forward scattering (FSC) values measured by flow cytometry verified the reduced size of shock cells, while the internal structure of shock cells remained unchanged (Figure 2E), suggesting that shock cells have no proliferation activity.

We further evaluated the cellular activity of the shock cells. Scanning electron microscopy (SEM) (Figure S7) revealed that shock cells adopted a spherical structure and a rougher cell surface in comparison to living cells. After being co-cultured with the HepG2 cells, M@TPE-s COF-Au@Cisplatin carrier cells still retained an oval structure (Figure 2F, left). However, under 808-nm laser irradiation, M@TPE-s COF-Au@Cisplatin was ruptured or collapsed, releasing the TPE-s COF-Au@Cisplatin carrier (Figure 2F, right). Subsequently, fluorescent staining showed that almost all shock cells were PI-labelled (propidium iodide, indicating dead cells) without showing the fluorescent signal of intact calmodulin AM (indicating live cells). In contrast, most live cells in the control group showed the intact Calcein-AM fluorescent signal, and very few were labeled with PI (Figure 2G), further indicating that the TPE-s COF-Au@Cisplatin nanozyme with HepG2 cell-specific fusion was successfully prepared. Next, we investigated the glucose oxidase-mimicking ability of the Au NPs in M@TPE-s COF-Au@Cisplatin carrier by using a DNS reagent kit (Ghose method) to measure the time-resolved changes in glucose concentration after nanozymes were added into aqueous glucose solution. As depicted in Figure 2H, M@TPE-s COF-Au@Cisplatin carrier decreased the glucose concentration significantly with prolonged incubation due to GOx-like catalytic activity of hosted Au NPs. In contrast, the hypoxic conditions do not have much effect on the catalytic effect of the nanozymes.

To verify the location of lipophilic TPE-s COF-Au@Cisplatin nanozyme after fusion with HepG2 cells, the HepG2 cells after co-culture were fixed. As illustrated in Figure 2I, the high-resolution transmission electron

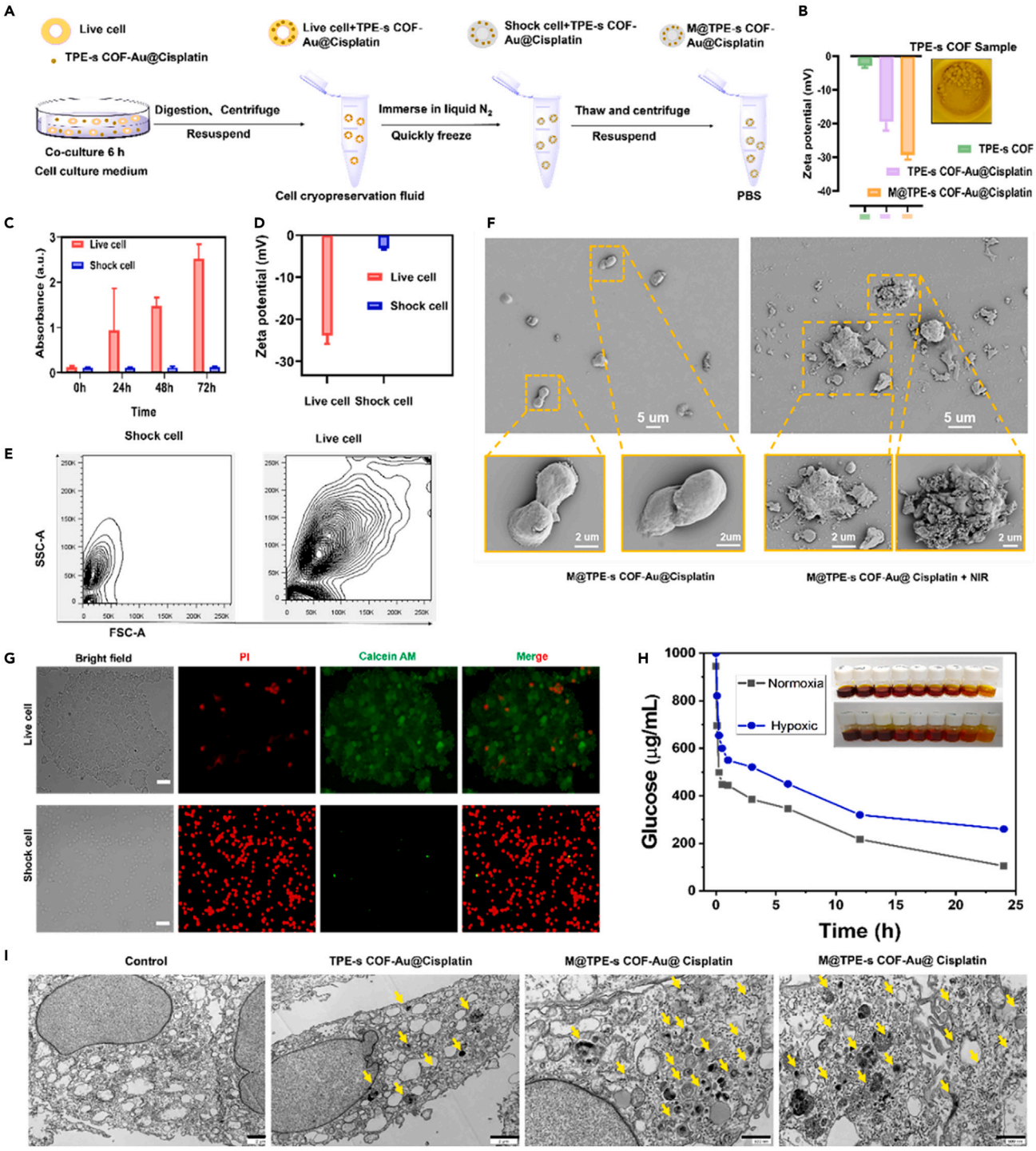

Figure 2. Synthesis and characterization of M@TPE-s COF-Au@Cisplatin nanozymes

(A) Schematic illustration of the preparation of monodisperse M@TPE-s COF-Au@Cisplatin nanozymes.

(B) Zeta potentials of TPE-s COF, TPE-s COF-Au@Cisplatin, and M@TPE-s COF-Au@Cisplatin samples (inset is the digital photo of TPE-s COF sample).

(C) Thiazolyl blue tetrazolium bromide (MTT) assay for the analysis of the viability of live and shock cells (n = 3).

(D) Zeta potential of live and shock cells.

(E) Flow cytometry analysis of live and shock cells at the same voltage (FSC, forward scatter; SSC, side scatter).

(F) SEM images of cell membrane-specific fusion TPE-s COF-Au@Cisplatin nanozymes with and without laser irradiation (808 nm, 1.0 W cm^{-2}) for 5 min.

Figure 2. *Continued*
(G) LIVE/DEAD cell viability kit for the analysis of live and shock cells (Calcein-AM: live cells; PI: shock cells). (Scale bar, 25 μm).
(H) Time-dependent GOx-like activity of M@TPE-s COF-Au@ Cisplatin nanozyme under normoxia and hypoxic conditions, n = 5.
(I) HR-TEM images of different groups of materials co-cultured with HepG2 cells for 6 h (Scale bars, 2 μm (Two pictures on the left) and 500 nm (Two pictures on the right).

microscopy (HRTEM) images showed that some nanozyme entered the cell and bound to the HepG2 cell membrane, whereas a few aggregated nanozyme (as indicated by the yellow arrow) did not enter the nucleus. This finding corroborates well with the results in Figure 2F that nanozyme was released after the rupture of the HepG2 cell membrane under laser irradiation. To sum up, the lipophilic TPE-s COF-Au@Cisplatin nanozyme displayed superb biocompatibility and could fuse well with HepG2 cells. Moreover, M@TPE-s COF-Au@Cisplatin carrier coupled with laser irradiation exerts a strong inhibitory effect on HepG2 cells.

In vitro cytotoxicity and cellular uptake of M@TPE-s COF-Au@Cisplatin nanozyme

To assess the *in vitro* endocytic and cytotoxic properties of M@TPE-s COF-Au@Cisplatin nanocomposite, we co-cultured M@TPE-s COF-Au@Cisplatin with model HepG2 cells for 6 h. The blue fluorescence of TPE-s COF on HepG2 cells was tracked by confocal microscopy, which was highly consistent with the red fluorescence of the cell membrane fluorescent probe DiI, further indicating that M@TPE-s COF-Au@Cisplatin was endocytosed and fused to the cell membrane (Figure 3A). This corroborates well with the HRTEM results (Figure 2I). In addition, we co-incubated TPE-s COF-Au with HepG2 cells for different times (2 h, 4 h, 6 h, 8 h, and 12 h) to determine the period with the maximum uptake. The fluorescence was tracked *in vivo* by flow cytometry. Compared with other groups, the fluorescence of cells after 6 h incubation was strong (Figure 3B), indicating the high uptake of TPE-s COF-Au carrier by HepG2 cells. We then used MTT assay (Figure S8) and Annexin V-FITC apoptosis assay (Figure 3C) to probe the cytotoxic and photothermal effects of different groups on HepG2 cells cultured *in vitro*. It was found that the TPE-s COF-Au group produced very low cytotoxicity even after incubation at a concentration of up to 200 μg mL^{-1} for 48 h, whereas the laser-irradiated groups showed enhanced apoptosis. Among them, the M@TPE-s COF-Au@ Cisplatin + near-infrared (NIR) group could efficiently kill cancer cells by combining chemotherapy and photothermal therapy, which was consistent with the results obtained by the MTT method. In addition, the mechanism of the anticancer effect of different groups at different stages of the cell cycle was evaluated by flow cytometry. Cisplatin induces DNA damage and a slight degree of G2/M phase arrest leading to the apoptosis of proliferating cells.[38] The TPE-s COF-Au@Cisplatin group triggered cell division and boosted the S phase compared to the untreated control cells. Combined treatment with M@TPE-s COF-Au@Cisplatin + laser group exhibited lower percentages of cells in the G0/G1 and higher ones in the G2/M phase (Figures 3D and 3E). These results suggest that M@TPE-s COF-Au@Cisplatin + laser exerted a cytostatic effect. Moreover, M@TPE-s COF-Au@ Cisplatin + laser treatment significantly suppressed the migration abilities of HepG2 cells (Figure S9).

To evaluate the *in vitro* immuno-stimulation of HepG2 cells by our nanozyme, the cytokines released by HepG2 cells were tested by enzyme linked immunosorbent assay (EILSA). M@TPE-s COF-Au@ Cisplatin + laser group induced the most efficient secretion of tumor necrosis factor alpha (TNF-α) and interleukin-1β (IL-1β) compared to control groups, revealing the efficient activation of T cell responses. Besides, there were no obvious changes in biomarker expression in the laser group (Figures 3F and 3G). We also observed that the levels of IL-10 were alleviated in culture supernatants of HepG2 cells across all treatments, especially for M@TPE-s COF-Au@Cisplatin + laser group (Figure 3H). The above results indicated that M@TPE-s COF-Au@Cisplatin group could weaken the tumor immunosuppressive microenvironment.

To assess the glucose oxidase-mimicking ability of the Au NPs in TPE-s COF, we measured the concentrations of intracellular glucose after treatment. The glucose concentration decreased steadily in a concentration-dependent manner, of which the relative levels dropped by ~75% at 200 μg/mL (Figure 3I). It has been documented that the conversion of glucose into lactic acid generates ATP that provides a survival advantage to cancer cells.[39,40] The extracellular lactate and intracellular ATP level significantly reduced for TPE-s COF-Au group due to catalytic glucose depletion (Figures 3J and 3K), indicating that the Au NPs maintained the excellent and comparable glucose oxidase-mimicking ability. As shown in Figure 3L, many green live cells can be detected from the confocal images, with a small number of apoptotic and/or necrotic cells in the control group. Under 1 W cm^{-2} laser irradiation, an increased area of red-stained cells was observed,

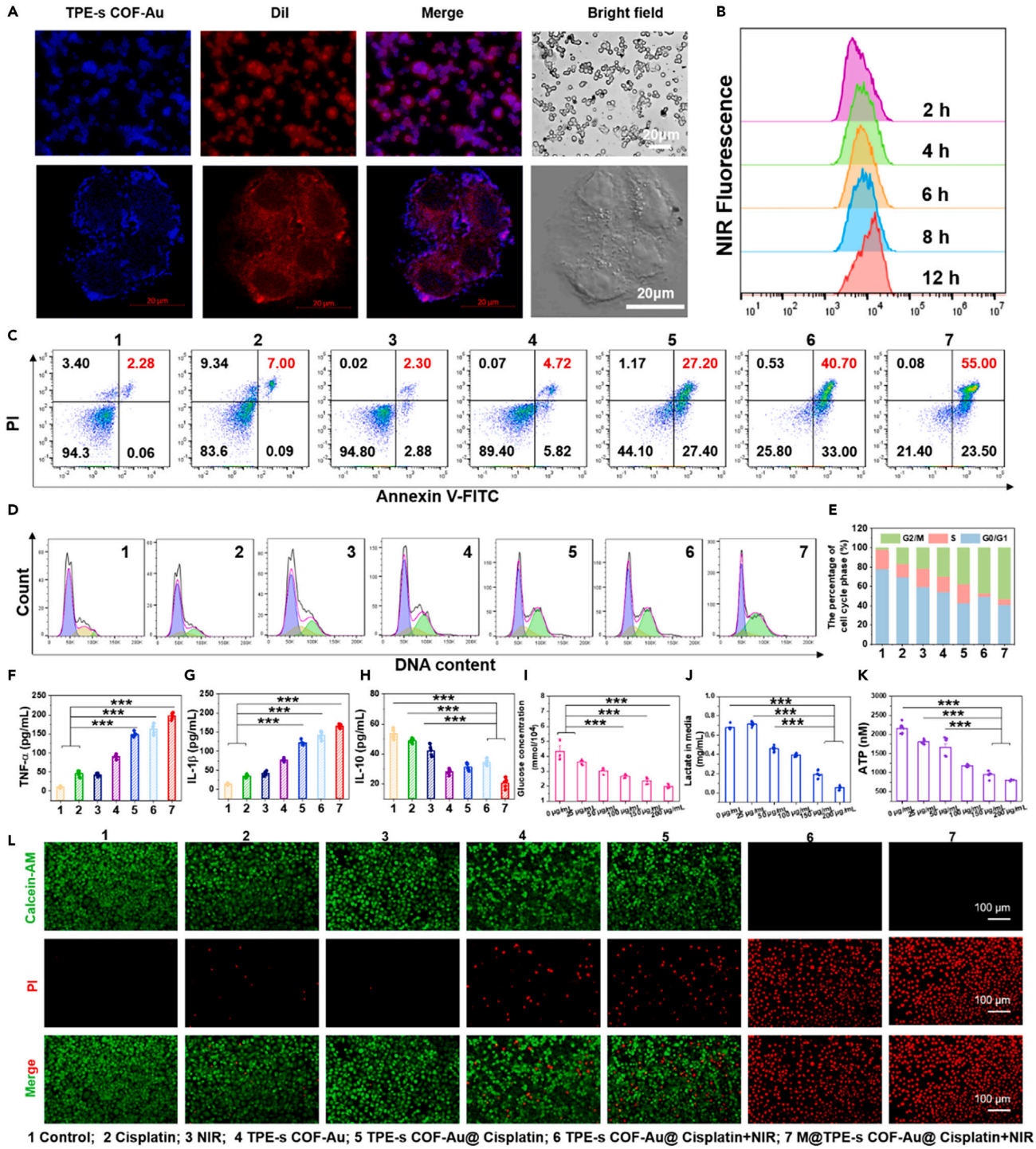

Figure 3. *In vitro* cellular uptake and PTT of M@TPE-s COF-Au@Cisplatin nanozymes

(A) CLSM images of TPE-s COF-Au incubated with HepG2 cells for 6 h, DiI (red fluorescent probe for cell membrane) stained cell membranes (Scale bars 20 μm).

(B) Flow cytometry detects the fluorescence intensity of TPE-s COF-Au after incubation with HepG2 cells at different times (2h, 4h, 6h, 8h, 12h).

(C) Annexin V-FITC apoptosis detects apoptosis of different groups of materials (n = 3) with/without laser irradiation (808 nm, 1.0 W cm^{-2}) for 5 min. The four areas represent the different phases of the cells: necrotic phase, late-stage apoptotic phase, early apoptotic phase, and liver phase, respectively.

(D) Effects of different treatments on the cell cycle in HepG2 cells.

Figure 3. *Continued*

(E) Percentage of cells cycle phase distribution (%) in HepG2 cells.

(F–H) The levels of (f) TNF-α, (g) IL-1β, and (h) IL-10 after the administration of different groups *in vitro*.

(I–K) Concentrations of (i) intracellular glucose, (j) extracellular lactic acid, and (k) intracellular ATP for HepG2 cells incubated with different concentrations of TPE-s COF-Au for 24 h.

(L) Fluorescence images of HepG2 cells incubated with different groups of materials with or without 808 nm laser irradiation. The viable and dead cells were dyed using Calcein-AM and PI, respectively. Statistical significance was calculated via one-way ANOVA with Tukey's post hoc test. Data are given as means ± SD. ***$p \leq 0.001$.

indicating that the M@TPE-s COF-Au@Cisplatin nanozyme group can act as a heat medium for efficient hyperthermia of cancer cells.

Fluorescence distribution of M@TPE-s COF-Au@Cisplatin nanozyme in tumor-bearing mice

Thanks to the highly emissive TPE-s COF, the bio-distribution of each sample was assessed by tracking the fluorescence of COF in isolated organs after intravenous injection of the samples into tumor-bearing mice via the tail vein. The *in vitro* imaging system (IVIS) in Figure 4A showed that TPE-s COF-Au@Cisplatin and M@TPE-s COF-Au@Cisplatin groups exhibited strong fluorescence under 430 nm excitation. To evaluate the *in vivo* distribution of TPE-s COF-Au@Cisplatin and M@TPE-s COF-Au@Cisplatin groups in tumor-bearing mice, *in vivo* fluorescence changes were assessed by tracking the fluorescence of TPE-s COF in the mice model. Intense fluorescence signals were observed in the tumor sites of the mice in the TPE-s COF-Au@Cisplatin and M@TPE-s COF-Au@Cisplatin groups (Figure 4B), indicating that the M@TPE-s COF-Au@Cisplatin nanozymes aggregated at the tumor sites. After 6 h, the *in vivo* imaging of the mice in the M@TPE-s COF-Au@Cisplatin group showed the strongest fluorescence, which was observed even after 96 h. Figure 4C shows the real-time change curve of fluorescence intensity *in vivo* in TPE-s COF-Au@ Cisplatin and M@TPE-s COF-Au@Cisplatin groups. After 3 days, mice were euthanized and tumors and major organs (heart, liver, spleen, lung, kidney, brain) were collected for fluorescence imaging. It was found that the fluorescence accumulated in the tumor and liver of the M@TPE-s COF-Au@Cisplatin group was significantly higher than that in the TPE-s COF-Au@ Cisplatin -treated mice (Figures 4D and 4E). In addition, we further verified live cells and M@TPE-s COF-Au@ Cisplatin cells and found that shock cells have a strong fluorescence at the tumor site (Figure 4F), indicating that M@TPE-s COF-Au@Cisplatin nanozymes achieve effective accumulation and strong targeting ability to tumors.

In vivo antitumor efficiency of COF nanozyme on tumor-bearing mice

We further investigated the photothermal effect *in vitro*. Under 808 nm laser irradiation (1 W cm^{-2}) for 5 min, the PBS solution showed a slight temperature change (Figures S10 and S11), while the temperature of TPE-s COF-Au@Cisplatin and M@TPE-s COF-Au@ Cisplatin group reached 54.2°C, and 55.6°C, respectively, indicating the TPE-s COF-Au@Cisplatin and M@TPE-s COF-Au@Cisplatin nanozymes had significant photothermal therapy (PTT) effects *in vitro*. Intrigued by this, we for the first time sought to perform the *in vivo* drug-delivery and starvation/chemo/photothermal combination therapy of M@TPE-s COF-Au@Cisplatin group in nude mice with a HepG2 cell xenograft tumor model.[41–43] To comprehensively evaluate the combined antitumor efficiency of TPE-s COF-Au@Cisplatin and M@TPE-s COF-Au@Cisplatin nanozymes, we monitored the experiment for 27 days (Figure S12), and tumor-bearing mice were randomly divided into the following 7 groups (n = 6): PBS, Cisplatin, laser, TPE-s COF-Au, TPE-s COF-Au@Cisplatin, TPE-s COF-Au@Cisplatin +laser, and M@TPE-s COF-Au@Cisplatin + laser. Not surprisingly, under 808 nm laser irradiation, the temperatures at the tumor site in the TPE-s COF-Au@Cisplatin +laser and the M@TPE-s COF-Au@Cisplatin +laser nanozyme group rapidly increased to 41.0°C, which was high enough to engender severe mortality of cancer cells.[44–46] Infrared thermal imaging (Figure 5A) and photothermal curves (Figure S13) showed that the temperature of the tumor site gradually increased in the TPE-s COF-Au@Cisplatin and M@TPE-s COF-Au@Cisplatin nanozyme groups with the extended laser irradiation time. The temperature of the tumor site in the TPE-s COF-Au@Cisplatin group reach 45.0°C, while that in the M@TPE-s COF-Au@Cisplatin nanozyme group reach 48.2°C, which is presumably due to the superb photothermal properties of Au NPs.[47,48] The thermal curves of the TPE-s COF-Au@Cisplatin and M@TPE-s COF-Au@Cisplatin nanozyme groups were similar, while the temperature of M@TPE-s COF-Au@Cisplatin group was significantly higher than that of the TPE-s COF-Au@Cisplatin group, mainly due to the specific targeting effect of HepG2 cells as a new nanozyme carrier after encapsulation. More importantly, the photothermally prepared Au was bound to TPE-s COF, and the Au NPs exerted a photothermal therapeutic effect on the tumor site, achieving a combined therapeutic effect and highly efficient tumor inhibition.

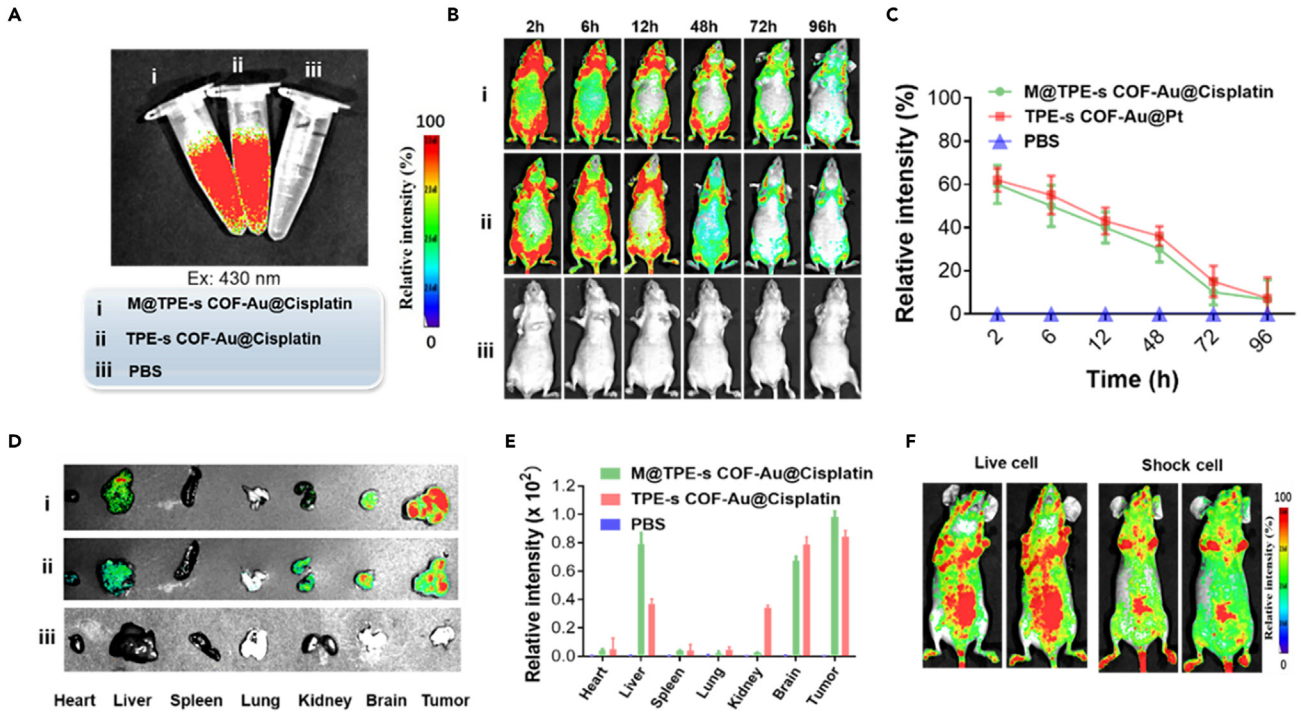

Figure 4. *In vivo* fluorescence imaging and fluorescence characteristics

(A) Fluorescence images of PBS, TPE-s COF-Au@ Cisplatin, M@TPE-s COF-Au@Cisplatin after the addition of the sample to the medium (ex: 430 nm).

(B) *In vivo* fluorescence images of HepG2-bearing mice at different times after intravenous injection of TPE-s COF-Au@Cisplatin, M@TPE-s COF-Au@Cisplatin, and PBS (ex: 430 nm).

(C) *In vivo* fluorescence intensity at different times after administration.

(D) Histo-fluorescence images of tumor-bearing mice after euthanasia three days after tail vein administration.

(E) fluorescence intensities of major organs and tumors after administration.

(F) *In vivo* fluorescence distribution of live cells and shock cells 4 h after tail vein administration of M@TPE-s COF-Au@ Cisplatin nanozyme. Each data point represents the average and SD (one above and one below the error bars) obtained from three different analyses in a single experiment.

The exceptional *in vitro* photothermal effect propelled us to probe the combined therapeutic effect of each nanozymes *in vivo*. Dosing and laser irradiation were performed every three days, and mice's body weight, tumor volume, and size were tracked (Figures S14, 5B, and 5C). Tumor volume changes of these groups during the 27-day treatment were recorded separately. In groups 1 and 4, tumor volume increased rapidly without laser irradiation. Compared with the tumor volume in groups 1, 2, and 3, the volume in groups 4 and 5 was slightly smaller, but there was no statistical significance, indicating that laser irradiation or chemotherapy alone cannot induce the anti-tumor effect. The treatment effect of group 5 was significantly better than that of group 1, and the tumor inhibition rate exceeded 50%, which is presumably due to the high drug-loading of TPE-s COF-Au (Figure 5D). Similar tumor growth kinetics indicated that TPE-s COF-Au exhibited a negligible antitumor effect. In contrast, the TPE-s COF-Au@Cisplatin + laser treatment substantially inhibited tumor growth under 808 nm laser irradiation, exhibiting a high inhibition rate of over 90% (Figure 5E). Considering the Au NPs -induced glucose deprivation process and cut down the energy and nutrition, our results further validated that M@TPE-s COF-Au@Cisplatin nanozyme groups could possess regulates tumor cells glucose metabolism to enhance anticancer activity. It is worth noting that the M@TPE-s COF-Au@Cisplatin +laser treatment group showed the best antitumor effect with an exceedingly high inhibition rate of 100%, and the tumor completely disappeared after 27 days of starvation/chemo/photothermal synergistic treatment (Figure 5F). M@TPE-s COF-Au@Cisplatin + laser treatment group also significantly extended the overall survival rates of the HepG2-bearing mice due to their extraordinary antitumor effect over the control groups (Figure 5G). In addition, all tumors were collected and weighed on day 27 after the treatment, and tumor mass was consistent with that obtained based on tumor growth curves and tumor volume (Figures 5H and 5C).

To further verify that cisplatin causes DNA damage and activates the apoptosis signal transduction pathway,[49] we tested the effect of nanozymes on the γ-H2AX/Bcl-2/caspase-3/Bax signaling pathways.

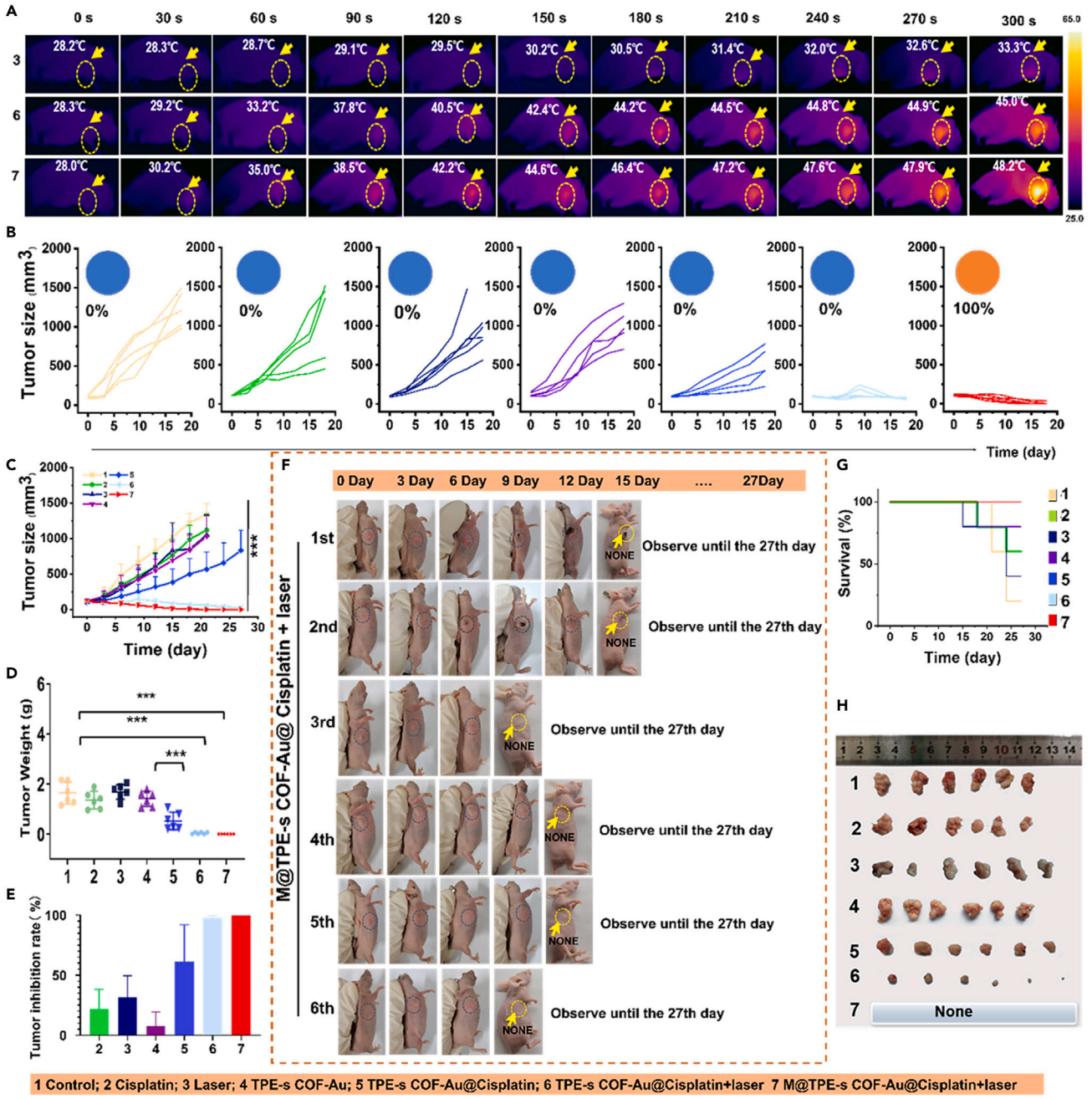

Figure 5. Antitumor effect *in vivo*

(A) Thermal imaging of HepG2 tumor-bearing mice in PBS, TPE-s COF-Au@ Cisplatin, M@TPE-s COF-Au@Cisplatin groups (200 μL, 1.0 mg mL^{-1}; 808 nm laser irradiation for 5 min).

(B and C) Individual and (c) average tumor growth curves of experimental mice (n = 5) in different treatment groups (pie chart represents the cure rate).

(D) Tumor weights of extracted tumors from different groups after 27 days of treatment.

(E) Tumor inhibition rate of HepG2 tumor-bearing mice in different treatment groups. Data are presented as mean ± standard deviation (n = 6).

(F) Photographs of mice and tumors for the M@TPE-s COF-Au@Cisplatin+ laser treatment group during the 27 days.

(G) Survival curves of HepG2 tumor-bearing mice in each group (n = 5) which underwent different treatments.

(H) Tumor photographs of dissected tumor-bearing mice after 27 days of treatment in each group (n = 6). Statistical significance was calculated via one-way ANOVA with Tukey's post hoc test. Data are given as means ± SD. ***$p \leq 0.001$.

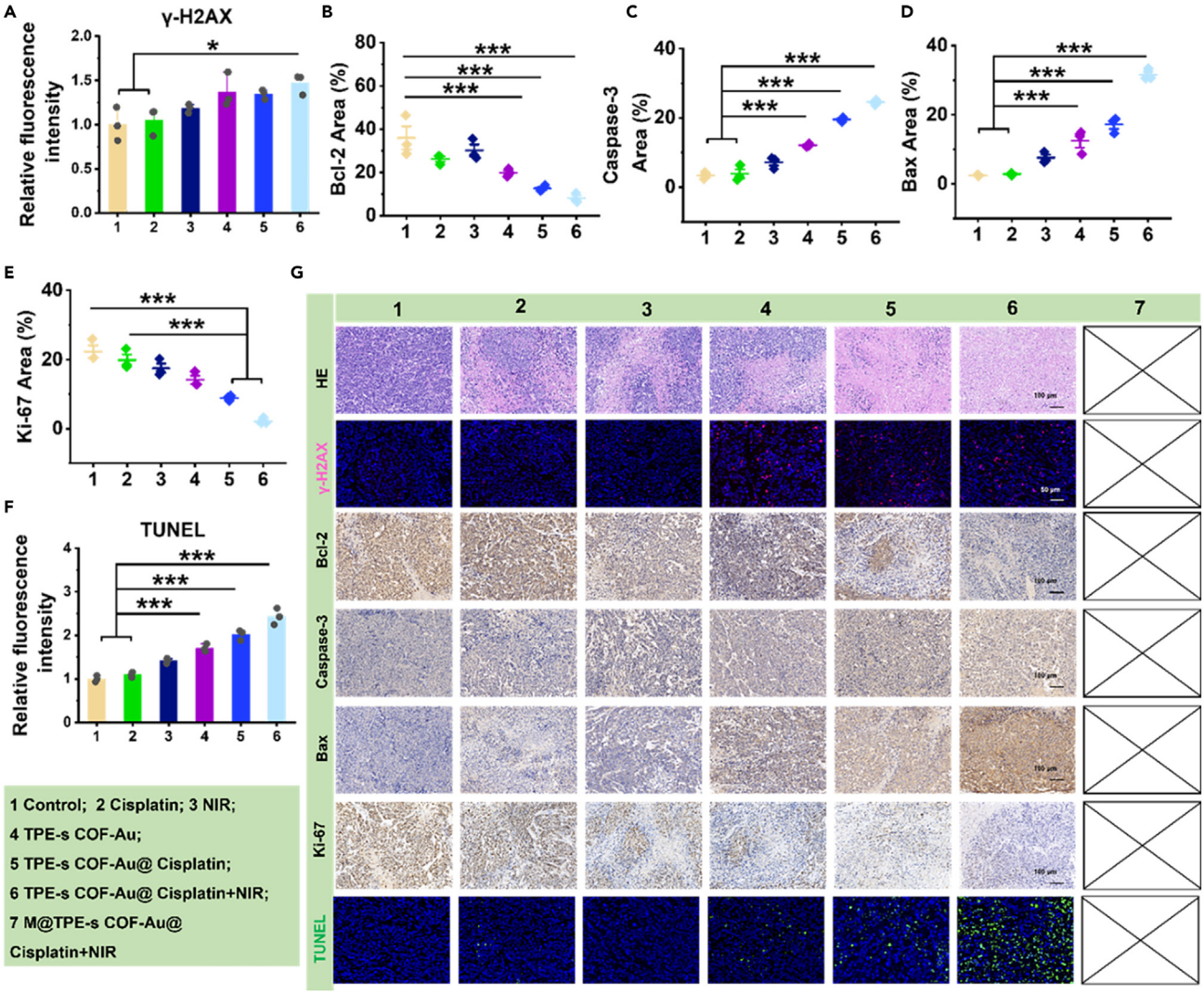

Figure 6. The apoptosis signal transduction pathway

(A–E) Semi-quantification of γ-H2AX and percentage of (b) Bcl-2-positive, (c) Caspase-3-positive, (d) Bax -positive and (e) Ki-67-positive cells in histological sections of different treatment groups.

(F) TUNEL expression in tumor sections.

(G) Representative images of H&E staining, immunofluorescence images of γ-H2AX and TUNEL, immuno-histochemical staining images of Ki-67, Bcl-2, caspase-3, and Bax on the tumor slices. Statistical significance was calculated via one-way ANOVA with Tukey's post hoc test. Data are given as means ± SD. *$p \leq 0.05$ and ***$p \leq 0.001$.

In the γ-H2AX assay, both TPE-s COF-Au@Cisplatin and TPE-s COF-Au@Cisplatin +laser groups showed a significant increase in γ-H2AX (Figure 6A). The level of Bcl-2 in the TPE-s COF-Au@Cisplatin and TPE-s COF-Au@Cisplatin + laser groups was significantly lower than that of the control group (Figure 6B). M@TPE-s COF-Au@Cisplatin-mediated upregulation of caspase 3 and Bax activation was further confirmed in tumor tissues compared with laser and the TPE-s COF-Au group alleviated this upregulation (Figures 6C and 6D). To further investigate the inhibition of tumor cell proliferation, H&E and Ki67 staining of tumor tissues after TPE-s COF-Au@Cisplatin + laser treatment confirmed the successful destruction of tumor cells and reduced proliferative capacity (Figures 6E and 6G). Additionally, TUNEL staining further showed many apoptotic tumor cells in the TPE-s COF-Au@ Cisplatin and TPE-s COF-Au@Cisplatin +laser groups, but few apoptotic tumor cells in the laser and TPE-s COF-Au groups with almost no apoptotic cell in the control group was observed (Figures 6F and 6G). Above all, TPE-s COF-Au mediated (M@TPE-s COF-Au@Cisplatin group) targeted starvation/chemo/photothermal combination therapy showed the most significant synergistic effect on tumor growth inhibition.

Subsequently, we collected hepatocellular carcinoma (HCC) cells from two other different sources (HCCLM3, MHCC-97H) and constructed mice models for *in vivo* combined therapy experiments. To directly evaluate the combined antitumor efficiency of M@TPE-s COF-Au@Cisplatin nanozymes, we monitored the experiment for 27 days (Figure 7A), and tumor-bearing mice were randomly divided into the following 2 groups (n = 5): Control and M@TPE-s COF-Au@Cisplatin + laser. Then, on the 6th day after the three injections, three of the five treated mice had no tumor, and no new tumors appeared after a long time (Figures 7B and 7C). All tumors were collected and weighed on day 27 after the treatment, and tumor mass was consistent with that obtained based on tumor volume (Figures 7D–7G). It is worth noting that after the fourth administration, the tumor completely disappeared, which further verified the experimental therapeutic effect of M@TPE-s COF-Au@Cisplatin nanozyme. Furthermore, after the third treatment (Figures 7H–7K), we performed H&E staining on the tumor of each mouse and found that the M@TPE-s COF-Au@Cisplatin + laser group was different from the control group, mostly round, small, and some small fusiform, with certain atypia. The tumor cells in the M@TPE-s COF-Au@Cisplatin + laser group were tightly arranged and diffusely distributed, without obvious nested structure and obvious tumor tissue necrosis. In addition, no significant changes in body weight were observed during treatment with M@TPE-s COF-Au@Cisplatin, and hematoxylin and eosin (H&E) staining of major organs showed no obvious histological damage when compared with the control group, which indicated that the therapeutic did not induce significant system toxicity. These results highlight the importance of the M@TPE-s COF-Au@Cisplatin nanozymes for targeted drug delivery and the inhibition of tumor growth.

Safety is of utmost significance before the therapeutic implementation of TPE-s COF-Au nanozymes in the body. During the treatment period, the weight change of mice is an important indicator of the toxicity of nanozymes. Notably, only one mouse in the Cisplatin group died during the treatment process. In addition, their weight did not fluctuate significantly (Figure S14), which is indicative of the excellent biocompatibility of nanozymes. As shown in Figure 8A, after incubating TPE-s COF-Au and M@TPE-s COF-Au in red blood cells at different concentrations for 4 h, both nanozymes manifested negligible percent hemolysis ratio (<2%), suggesting the high blood biocompatibility of the nanozymes. Inspired by the good biocompatibility *in vitro*, we examined the safety profiles of nanozymes by blood biochemistry assay and H&E staining of the main organs (heart, liver, spleen, lung, and kidney). All the biochemical parameters in serum tests remained at a normal range in TPE-s COF-Au and control group (Figure 8B). For the mice treated with cisplatin alone, the liver of mice presented vacuolar degeneration and renal cells with marked ballooning degeneration, indicating the nephrotoxicity and liver damage. By contrast, no obvious damage to major organs was found in other groups (Figure 8C), revealing that TPE-s COF-Au@Cisplatin and M@TPE-s COF-Au@Cisplatin nanozymes could alleviate side effects of cisplatin *in vivo* and present satisfactory security.

DISCUSSION

The past decade has witnessed a significant progress of COF in the combination of photothermal therapy (PTT) and chemotherapy.[15–18] Combination therapies, especially chemo/photothermal combination therapy, are advantageous over monotherapies.[50–54] Since they can not only maintain the non-invasiveness, low toxicity, and convenient administration of PTT[55,56] but also improve the non-selectivity of traditional chemotherapy, multi-drug resistance, and other issues. Regardless of the great strides, the poor biocompatibility, bio-interfacial properties, and lack of target-specificity severely restrain the clinical implementation of COF in combination therapy. To this end, cancer cells, which have tropism and homing ability to diseased regions, provide a viable solution. Cancer cell membranes have a bimolecular-phospholipid lipophilic structure, which enables some lipophilic nanoparticles to bind to the specificity of cancer cell membranes. Lipophilic nanocarriers fusing cancer cell membranes can endow NPs with good biocompatibility, bio-interface properties, and specific targeting effects. Inspired by this, autologous tumor cell-anchored AIEgen-based COF nanomedicines were constructed and covered with unique invisible cell armors. It endows TPE-s COF with good biocompatibility and specific targeting effects, which enhances the low targeting efficiency of COF.

When the inactivated M@TPE-s COF-Au@Cisplatin nanozyme was irradiated by laser, the M@TPE-s COF-Au@Cisplatin nanozyme was cleaved, thereby releasing the TPE-s COF-Au and cisplatin prodrug to exert their therapeutic effect. The spatiotemporal release of cisplatin at the tumor target sites was achieved. The released cisplatin-loaded TPE-s COF-Au nanozymes infiltrated the deep tumors after laser irradiation of

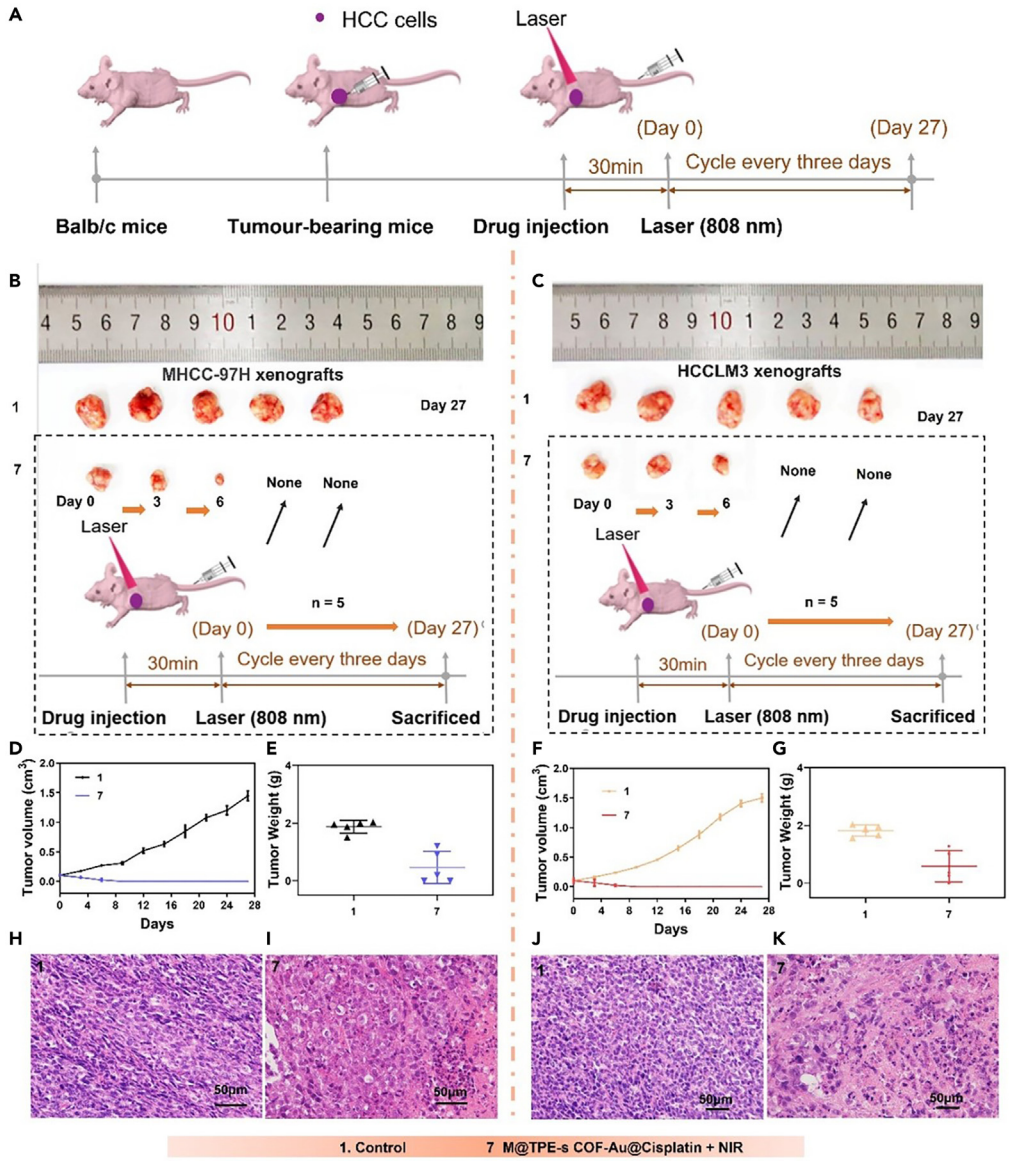

Figure 7. *In vivo* M@TPE-s COF-Au@Cisplatin nanozyme further enhances targeting and specific recognition of starvation/chemo/photothermal combination therapy

(A) Schematic diagram of subcutaneous tumor model establishment and NIR light-triggered combined therapy.
(B and C) Schematic diagram of subcutaneous tumor model establishment and NIR light-triggered combined therapy. Tumor photographs of dissected tumor-bearing mice after 27 days of treatment in the control group (n = 5).
(D and F) Tumor volume change curve of experimental mice and (E, G) Mean tumor weights (n = 5) in different treatment groups.
(H–K) HE analysis of extracted tumors from different groups after 6 days of treatment (Scale bars 50 μm). Data in (d) and (f) are presented as mean ± standard deviation (n = 5).

tumor-site cells. The enhanced deep-tumor starvation therapy and chem-photothermal therapies solved the small-molecule drug release in COF. Overall, a novel Au-based AIEgen COF nanozyme was developed for dual imaging and targeted starvation/chemo/photothermal combination therapy of hepatocellular carcinoma. Au-based AIEgen COF nanozyme consisted of the navigation and targeting system, photothermal system, and drug-loading system. Tumor cells acted as engines and drug storehouses for the target-driven and TPE-s COF-Au delivery. TPE-s COF and encapsulated Au NPs had photothermal and AIE fluorescence tracking properties. Furthermore, prodrug cisplatin can be loaded in TPE-s COF-Au carrier. The resultant nanozymes displayed remarkable therapeutic effects. Cisplatin and TPE-s COF-Au nanozymes-treated

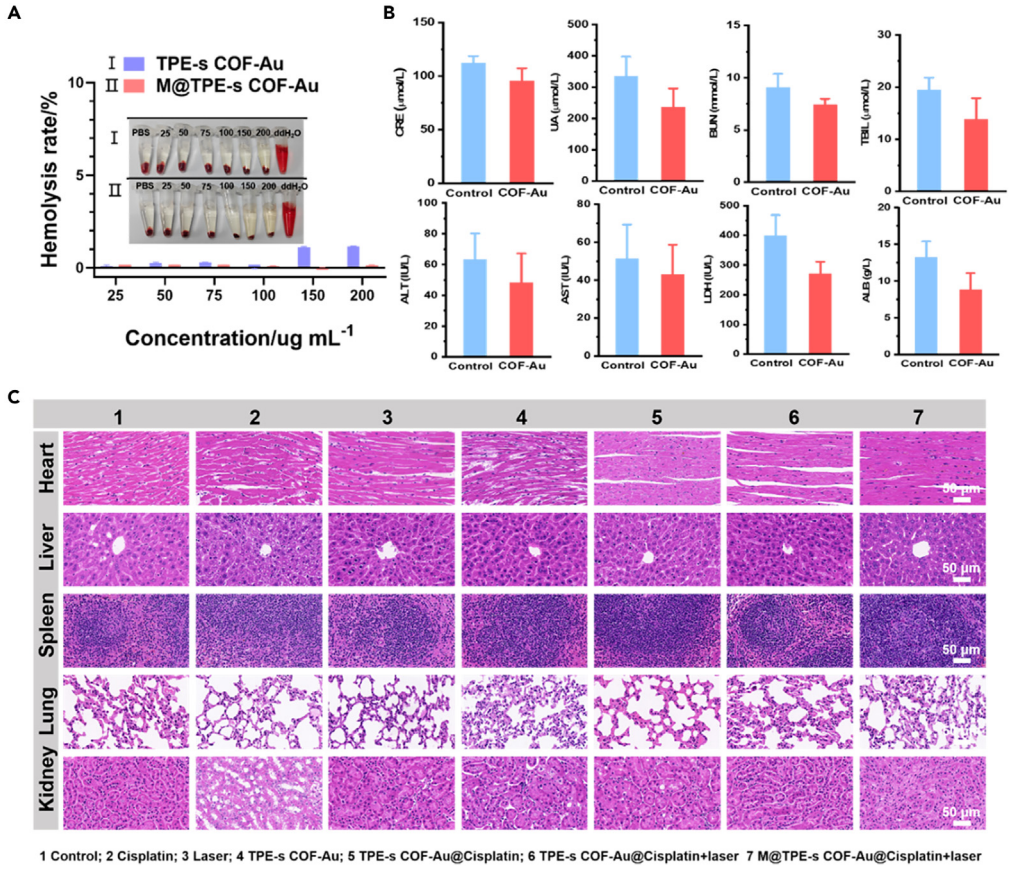

Figure 8. Biocompatibility evaluation of TPE-s COF-Au nanozymes

(A) Hemolysis characterization of TPE-s COF-Au and M@TPE-s COF-Au.

(B) Serum biochemistry data of mice with TPE-s COF-Au treatment.

(C) H&E images of the major organs of mice for different treatment groups. The scale bar = 50 μm.

groups showed the most efficient tumor growth inhibition among various groups. To further improve the therapeutic effect, the combined treatment group (M@TPE-s COF-Au@Cisplatin + laser treatment group) showed the strongest inhibitory effect on tumor growth (Figure 5E). Tumor weight graphs showed the effect of the combination therapy on day 27 (Figures 5D, 5H, and 7D–7G). Meanwhile, the weight loss of mice in each group was not obvious, indicating the low toxicity of the therapeutic drugs to animals (Figure S14). The results showed that the TPE-s COF-Au nanozymes based on the specificity of autologous tumor cells and aggregation-induced luminescence structures engender high therapeutic effects with enhanced targeting and specific recognition.

In conclusion, we have developed a novel M@TPE-s COF-Au@Cisplatin nanozyme as a theragnostic nanocarrier for dual imaging and targeted starvation/chemo/photothermal combination therapy of HCC. The M@TPE-s COF-Au@Cisplatin nanozyme eliminated the tumorigenicity of tumor cells by simple liquid nitrogen treatment and retained their structural integrity, which enables the TPE-s COF-Au@Cisplatin carrier to fuse into the HepG2 cell and home to the tumor site. In addition, the M@TPE-s COF-Au@Cisplatin nanozyme targeting can reduce the consumption of cisplatin during systemic circulation, thereby minimizing off-target effects. As a result, M@TPE-s COF-Au@Cisplatin nanozyme achieved exceptional *in vivo* antitumor effects. Notably, glucose oxidase-like Au NPs was able to accelerate the depletion of intratumoral glucose and enhanced strong NIR absorption. Remarkably, upon the modification with HepG2 cell-specific fusion TPE-s COF-Au, M@TPE-s COF-Au@Cisplatin nanozymes hold unique advantages over commonly used photothermal agents: strongly catalytic activity, high homologous targeting and specificity, long-term solution stability, high photothermal conversion efficiency, and superior aggregation degree of Au NPs at tumor sites. Importantly, co-validated in three animal models, coupled with additional functions

such as fluorescence imaging, and tumor targeting, this work paves a new path to access advanced COF nanozymes for starvation/chemo/photothermal combination therapy.

Limitations of the study

We construct an AIEgen-based COF nanozyme with autologous cell membrane-specific fusion and inherent luminescence for dual imaging and efficient chemo/photothermal combination therapy. More intriguingly, the specific role of COF encapsulated inside the cell membranes in brain targeting test has not been elucidated, and further investigation is currently underway in our laboratory.

STAR★METHODS

Detailed methods are provided in the online version of this paper and include the following:

- KEY RESOURCES TABLE
- RESOURCE AVAILABILITY
  - Lead contact
  - Materials availability
  - Data and code availability
- EXPERIMENTAL MODEL AND SUBJECT DETAILS
  - Animals and tumor models
  - Cell culture
- METHOD DETAILS
  - Synthesis of AIEgen-based COF (TPE-s COF)
  - Synthesis of TPE-s COF-Au
  - Synthesis of TPE-s COF-Au@Cisplatin
  - Synthesis of M@TPE-s COF-Au@ cisplatin
  - Preparation of shock cells
  - Cell uptake analysis
  - Cytotoxic studies of different materials
  - MTT experiment
  - Annexin V-FITC apoptosis detection experiment
  - Calcein-AM and PI staining analysis experiments
  - Animal and tumor models
  - *In vivo* and *in vitro* fluorescence imaging
  - Synergistic therapy *in vivo*
- QUANTIFICATION AND STATISTICAL ANALYSIS

SUPPLEMENTAL INFORMATION

Supplemental information can be found online at https://doi.org/10.1016/j.isci.2023.107348.

ACKNOWLEDGMENTS

This study was financially supported by the Basic and Clinical Collaborative Research Promotion Program of Anhui Medical University (No. 2021xkjT024) and the Ph.D. Start-up Fund of Anhui Medical University. The authors were grateful for financial support from the Anhui Provincial Institute of Translational Medicine Fund (No 2022zhyx-C13).

AUTHOR CONTRIBUTIONS

S.Z. and T.T. contributed equally to this work. H.W. and G.Z. designed the research; S.Z., T.T., T.M., J.W., D.H., Q.L., and J.Z. performed the research; All authors analyzed and interpreted the data; S.Z., T.T., and G.Z. wrote the paper.

DECLARATION OF INTERESTS

The authors declare that they have no known competing financial interests or personal relationships that could have appeared to influence the work reported in this paper.

Received: April 3, 2023
Revised: May 30, 2023
Accepted: July 6, 2023
Published: July 16, 2023

REFERENCES

1. Gong, X., Li, J., Tan, T., Wang, Z., Wang, H., Wang, Y., Xu, X., Zhang, Z., and Li, Y. (2019). Emerging approaches of cell-based nanosystems to target cancer metastasis. Adv. Funct. Mater. *29*, 1903441. https://doi.org/10.1002/adfm.201903441.

2. Martinez, J.O., Evangelopoulos, M., Brozovich, A.A., Bauza, G., Molinaro, R., Corbo, C., Liu, X., Taraballi, F., and Tasciotti, E. (2020). Mesenchymal stromal cell-mediated treatment of local and systemic inflammation through the triggering of an anti-inflammatory response. Adv. Funct. Mater. *31*, 2002997. https://doi.org/10.1002/adfm.202002997.

3. Maciel, M.M., Correia, T.R., Gaspar, V.M., Rodrigues, J.M.M., Choi, I.S., and Mano, J.F. (2021). Partial coated stem cells with bioinspired silica as new generation of cellular hybrid materials. Adv. Funct. Mater. *31*, 2009619. https://doi.org/10.1002/adfm.202009619.

4. Ci, T., Li, H., Chen, G., Wang, Z., Wang, J., Abdou, P., Tu, Y., Dotti, G., and Gu, Z. (2020). Cryoshocked cancer cells for targeted drug delivery and vaccination. Sci. Adv. *6*, eabc3013. https://doi.org/10.1126/sciadv.abc3013.

5. Zhao, Z., Fang, L., Xiao, P., Sun, X., Zhou, L., Liu, X., Wang, J., Wang, G., Cao, H., Zhang, P., et al. (2022). Walking dead tumor cells for targeted drug delivery against lung metastasis of triple-negative breast cancer. Adv. Mater. *34*, 2205462. https://doi.org/10.1002/adma.202205462.

6. Wang, T., Wang, D., Yu, H., Feng, B., Zhou, F., Zhang, H., Zhou, L., Jiao, S., and Li, Y. (2018). A cancer vaccine-mediated postoperative immunotherapy for recurrent and metastatic tumors. Nat. Commun. *9*, 1532. https://doi.org/10.1038/s41467-018-03915-4.

7. Altorki, N.K., Markowitz, G.J., Gao, D., Port, J.L., Saxena, A., Stiles, B., McGraw, T., and Mittal, V. (2019). The lung microenvironment: an important regulator of tumour growth and metastasis. Nat. Rev. Cancer *19*, 9–31. https://doi.org/10.1038/s41568-018-0081-9.

8. Fang, L., Zhao, Z., Wang, J., Zhang, P., Ding, Y., Jiang, Y., Wang, D., and Li, Y. (2020). Engineering autologous tumor cell vaccine to locally mobilize antitumor immunity in tumor surgical bed. Sci. Adv. *6*, eaba4024. https://doi.org/10.1126/sciadv.aba4024.

9. Frank, M.J., Khodadoust, M.S., Czerwinski, D.K., Haabeth, O.A.W., Chu, M.P., Miklos, D.B., Advani, R.H., Alizadeh, A.A., Gupta, N.K., Maeda, L.S., et al. (2020). Autologous tumor cell vaccine induces antitumor T cell immune responses in patients with mantle cell lymphoma: a phase I/II trial. J. Exp. Med. *217*, e20191712. https://doi.org/10.1084/jem.20191712.

10. Xu, J., Lv, J., Zhuang, Q., Yang, Z., Cao, Z., Xu, L., Pei, P., Wang, C., Wu, H., Dong, Z., et al. (2020). A general strategy towards personalized nanovaccines based on fluoropolymers for post-surgical cancer immunotherapy. Nat. Nanotechnol. *15*, 1043–1052. https://doi.org/10.1038/s41565-020-00781-4.

11. Zhang, Y., Ma, S., Liu, X., Xu, Y., Zhao, J., Si, X., Li, H., Huang, Z., Wang, Z., Tang, Z., et al. (2021). Supramolecular assembled programmable nanomedicine as in situ cancer vaccine for cancer immunotherapy. Adv. Mater. *33*, e2007293. https://doi.org/10.1002/adma.202007293.

12. Di Costanzo, G.G., Francica, G., and Pacella, C.M. (2014). Laser ablation for small hepatocellular carcinoma: State of the art and future perspectives. World J. Hepatol. *6*, 704–715. https://doi.org/10.4254/wjh.v6.i10.704.

13. Zhang, G., Li, X., Liao, Q., Liu, Y., Xi, K., Huang, W., and Jia, X. (2018). Water-dispersible PEG-curcumin/amine-functionalized covalent organic framework nanocomposites as smart carriers for in vivo drug delivery. Nat. Commun. *9*, 2785. https://doi.org/10.1038/s41467-018-04910-5.

14. Wang, K., Zhang, Z., Lin, L., Hao, K., Chen, J., Tian, H., and Chen, X. (2019). Cyanine-assisted exfoliation of covalent organic frameworks in nanocomposites for highly efficient chemo-photothermal tumor therapy. ACS Appl. Mater. Interfaces *11*, 39503–39512. https://doi.org/10.1021/acsami.9b13544.

15. Guan, Q., Zhou, L.L., Li, Y.A., Li, W.Y., Wang, S., Song, C., and Dong, Y.B. (2019). Nanoscale covalent organic framework for combinatorial antitumor photodynamic and photothermal therapy. ACS Nano *13*, 13304–13316. https://doi.org/10.1021/acsnano.9b06467.

16. Bhunia, S., Deo, K.A., and Gaharwar, A.K. (2020). 2D covalent organic frameworks for biomedical applications. Adv. Funct. Mater. *30*, 2002046. https://doi.org/10.1002/adfm.202002046.

17. Scicluna, M.C., Vella-Zarb, L., Vella-Zarb, and Liana. (2020). Evolution of nanocarrier drug-delivery systems and recent advancements in covalent organic framework–drug systems. ACS Appl. Nano Mater. *3*, 3097–3115. https://doi.org/10.1021/acsanm.9b02603.

18. Zhou, S., Meng, T., Hu, D., Zhu, Y., Huang, C., Song, M., Gao, S., and Zhang, G. (2022). Characteristic synthesis of a covalent organic framework and its application in multifunctional tumor therapy. ACS Appl. Bio Mater. *5*, 59–81. https://doi.org/10.1021/acsabm.1c01039.

19. Yang, L., Zhu, H., Zhao, R., Zhang, Z., Liu, B., Gong, H., Zhu, Y., Ding, H., Gai, S., and Feng, L. (2022). Tumor microenvironment activated glutathione self-depletion theranostic nanocapsules for imaging-directed synergistic cancer therapy. Chem. Eng. J. *450*, 138137. https://doi.org/10.1016/j.cej.2022.138137.

20. Zhao, R., Zhu, Y., Zhou, J., Liu, B., Du, Y., Gai, S., Shen, R., Feng, L., and Yang, P. (2022). Dual glutathione depletion enhanced enzyme catalytic activity for hyperthermia assisted tumor therapy on semi-metallic VSe(2)/Mn-CS. ACS Nano *16*, 10904–10917. https://doi.org/10.1021/acsnano.2c03222.

21. Zhu, Y., Wang, Z., Zhao, R., Zhou, Y., Feng, L., Gai, S., and Yang, P. (2022). Pt decorated Ti3C2Tx MXene with NIR-II light amplified nanozyme catalytic activity for efficient phototheranostics. ACS Nano *16*, 3105–3118. https://doi.org/10.1021/acsnano.1c10732.

22. Ma, J., Qiu, J., and Wang, S. (2020). Nanozymes for catalytic cancer immunotherapy. *ACS Appl.* Nano Mater. *3*, 4925–4943. https://doi.org/10.1021/acsanm.0c00396.

23. Comotti, M., Della Pina, C., Matarrese, R., and Rossi, M. (2004). The catalytic activity of "naked" gold particles. Angew. Chem. *43*, 5812–5815. https://doi.org/10.1002/ange.200460446.

24. Liu, C., Xing, J., Akakuru, O.U., Luo, L., Sun, S., Zou, R., Yu, Z., Fang, Q., and Wu, A. (2019). Nanozymes-engineered metal–organic frameworks for catalytic cascades-enhanced synergistic cancer therapy. Nano Lett. *19*, 5674–5682. https://doi.org/10.1021/acs.nanolett.9b02253.

25. Kornberg, M.D., Bhargava, P., Kim, P.M., Putluri, V., Snowman, A.M., Putluri, N., Calabresi, P.A., and Snyder, S.H. (2018). Dimethyl fumarate targets GAPDH and aerobic glycolysis to modulate immunity. Science *360*, 449–453. https://doi.org/10.1126/science.aan4665.

26. Kang, H., Buchman, J.T., Rodriguez, R.S., Ring, H.L., He, J., Bantz, K.C., and Haynes, C.L. (2019). Stabilization of liver and gold nanoparticles: preservation and improvement of plasmonic functionalities. Chem. Rev. *119*, 664–699. https://doi.org/10.1021/acs.chemrev.8b00341.

27. Cai, L., Hu, C., Liu, S., Zhou, Y., Pang, M., and Lin, J. (2020). A covalent organic framework-based multifunctional therapeutic platform for enhanced photodynamic therapy via catalytic cascade reactions. Sci. China Mater. *64*, 488–497. https://doi.org/10.1007/s40843-020-1428-0.

28. Fan, M., Han, Y., Gao, S., Yan, H., Cao, L., Li, Z., Liang, X.J., and Zhang, J. (2020). Ultrasmall gold nanoparticles in cancer diagnosis and

therapy. Theranostics *10*, 4944–4957. https://doi.org/10.7150/thno.42471.

29. Xu, W., He, W., Du, Z., Zhu, L., Huang, K., Lu, Y., and Luo, Y. (2021). Functional nucleic acid nanomaterials: development, properties, and applications. Angew Chem. Int. Ed. Engl. *60*, 6890–6918. https://doi.org/10.1002/anie.201909927.

30. Sun, Q., Aguila, B., Perman, J., Earl, L.D., Abney, C.W., Cheng, Y., Wei, H., Nguyen, N., Wojtas, L., and Ma, S. (2017). Postsynthetically modified covalent organic frameworks for efficient and effective mercury removal. J. Am. Chem. Soc. *139*, 2786–2793. https://doi.org/10.1021/jacs.6b12885.

31. Jiang, Q., Li, Y., Zhao, X., Xiong, P., Yu, X., Xu, Y., and Chen, L. (2018). Inverse-vulcanization of vinyl functionalized covalent organic frameworks as efficient cathode materials for Li–S batteries. J. Mater. Chem. A. *6*, 17977–17981. https://doi.org/10.1039/c8ta07008c.

32. Xu, H., Aizpurua, J., Ka'll, M., and Apell, P. (2000). Electromagnetic contributions to single-molecule sensitivity in surface-enhanced Raman scattering. Phys. Rev. E E. *62*, 4318–4324. https://doi.org/10.1103/physreve.62.4318.

33. Zhou, X., Huang, X., Qi, X., Wu, S., Xue, C., Boey, F.Y.C., Yan, Q., Chen, P., and Zhang, H. (2009). In situ synthesis of metal nanoparticles on single-layer graphene oxide and reduced graphene oxide surfaces. J. Phys. Chem. C *113*, 10842–10846. https://doi.org/10.1021/jp903821n.

34. Dursun, S., Yavuz, E., and Çetinkaya, Z. (2019). In situ reduction of chloroauric acid (HAuCl4) for generation of catalytic Au nanoparticle embedded triazine based covalent organic polymer networks. RSC Adv. *9*, 38538–38546. https://doi.org/10.1039/c9ra08822a.

35. Wang, P., Zhou, D., Kinraide, T.B., Luo, X., Li, L., Li, D., and Zhang, H. (2008). Cell membrane surface potential (psi0) plays a dominant role in the phytotoxicity of copper and arsenate. Plant Physiol. *148*, 2134–2143. https://doi.org/10.1104/pp.108.127464.

36. Yeung, T., Gilbert, G.E., Shi, J., Silvius, J., Kapus, A., and Grinstein, S. (2008). Membrane phosphatidylserine regulates surface charge and protein localization. Science *319*, 210–213. https://doi.org/10.1126/science.1152066.

37. Nishino, M., Matsuzaki, I., Musangile, F.Y., Takahashi, Y., Iwahashi, Y., Warigaya, K., Kinoshita, Y., Kojima, F., and Murata, S.I. (2020). Measurement and visualization of cell membrane surface charge in fixed cultured cells related with cell morphology. PLoS One *15*, e0236373. https://doi.org/10.1371/journal.pone.0236373.

38. Tartaglione, M.F., Eléxpuru Zabaleta, M., Lazzarini, R., Piva, F., Busilacchi, E.M., Poloni, A., Ledda, C., Rapisarda, V., Santarelli, L., and Bracci, M. (2021). Apoptotic mechanism activated by blue light and cisplatinum in cutaneous squamous cell carcinoma cells. Int. J. Mol. Med. *47*, 48. https://doi.org/10.3892/ijmm.2021.4881.

39. Gatenby, R.A., and Gillies, R.J. (2004). Why do cancers have high aerobic glycolysis? Nat. Rev. Cancer *4*, 891–899. https://doi.org/10.1038/nrc1478.

40. Lunt, S.Y., and Vander Heiden, M.G. (2011). Aerobic glycolysis: meeting the metabolic requirements of cell proliferation. Annu. Rev. Cell Dev. Biol. *27*, 441–464. https://doi.org/10.1146/annurev-cellbio-092910-154237.

41. Kaji, K., Nishimura, N., Seki, K., Sato, S., Saikawa, S., Nakanishi, K., Furukawa, M., Kawaratani, H., Kitade, M., Moriya, K., et al. (2018). Sodium glucose cotransporter 2 inhibitor canagliflozin attenuates liver cancer cell growth and angiogenic activity by inhibiting glucose uptake. Int. J. Cancer *142*, 1712–1722. https://doi.org/10.1002/ijc.31193.

42. Wang, S., Xu, M., Li, X., Su, X., Xiao, X., Keating, A., and Zhao, R.C. (2018). Exosomes released by hepatocarcinoma cells endow adipocytes with tumor-promoting properties. J. Hematol. Oncol. *11*, 82. https://doi.org/10.1186/s13045-018-0625-1.

43. Wang, L., Huang, W., and Zhan, J. (2019). Grape seed proanthocyanidins induce autophagy and modulate survivin in HepG2 cells and inhibit xenograft tumor growth in vivo. Nutrients *11*, 2983. https://doi.org/10.3390/nu11122983.

44. Jang, B., Park, J.Y., Tung, C.H., Kim, I.H., and Choi, Y. (2011). Gold nanorod-photosensitizer complex for near-infrared fluorescence imaging and photodynamic/photothermal therapy in vivo. ACS Nano *5*, 1086–1094. https://doi.org/10.1021/nn102722z.

45. Zhu, X., Feng, W., Chang, J., Tan, Y.W., Li, J., Chen, M., Sun, Y., and Li, F. (2016). Temperature-feedback upconversion nanocomposite for accurate photothermal therapy at facile temperature. Nat. Commun. *7*, 10437. https://doi.org/10.1038/ncomms10437.

46. Dong, Q., Wang, X., Hu, X., Xiao, L., Zhang, L., Song, L., Xu, M., Zou, Y., Chen, L., Chen, Z., and Tan, W. (2018). Simultaneous application of photothermal therapy and an anti-inflammatory prodrug using pyrene-aspirin-loaded gold nanorod graphitic nanocapsules. Angew Chem. Int. Ed. Engl. *57*, 177–181. https://doi.org/10.1002/anie.201709648.

47. Li, J., Han, J., Xu, T., Guo, C., Bu, X., Zhang, H., Wang, L., Sun, H., and Yang, B. (2013). Coating urchinlike gold nanoparticles with polypyrrole thin shells to produce photothermal agents with high stability and photothermal transduction efficiency. Langmuir *29*, 7102–7110. https://doi.org/10.1021/la401366c.

48. Song, L., Qiu, N., Huang, Y., Cheng, Q., Yang, Y., Lin, H., Su, F., and Chen, T. (2020). Macroscopic orientational gold nanorods monolayer film with excellent photothermal anticounterfeiting performance. Adv. Opt. Mater. *8*, 1902082. https://doi.org/10.1002/adom.201902082.

49. Siddik, Z.H. (2003). Cisplatin: mode of cytotoxic action and molecular basis of resistance. Oncogene *22*, 7265–7279. https://doi.org/10.1038/sj.onc.1206933.

50. Guan, Q., Wang, G.B., Zhou, L.L., Li, W.Y., and Dong, Y.B. (2020). Nanoscale covalent organic frameworks as theranostic platforms for oncotherapy: synthesis, functionalization, and applications. Nanoscale Adv. *2*, 3656–3733. https://doi.org/10.1039/d0na00537a.

51. Guan, Q., Zhou, L.L., Li, W.Y., Li, Y.A., and Dong, Y.B. (2020). Covalent organic frameworks (COFs) for cancer therapeutics. Chemistry *26*, 5583–5591. https://doi.org/10.1002/chem.201905150.

52. Liu, S., Zhou, Y., Hu, C., Cai, L., and Pang, M. (2020). Covalent organic framework-based nanocomposite for synergetic photo-chemodynamic-and immunotherapies. ACS Appl. Mater. Interfaces *12*, 43456–43465. https://doi.org/10.1021/acsami.0c12824.

53. Valenzuela, C., Chen, C., Sun, M., Ye, Z., and Zhang, J. (2021). Strategies and applications of covalent organic frameworks as promising nanoplatforms in cancer therapy. J. Mater. Chem. B *9*, 3450–3483. https://doi.org/10.1039/d1tb00041a.

54. Wan, X., Zhang, H., Pan, W., Li, N., and Tang, B. (2021). An enzyme nanopocket based on covalent organic frameworks for long-term starvation therapy and enhanced photodynamic therapy of cancer. Chem. Commun. *57*, 5402–5405. https://doi.org/10.1039/d0cc07544b.

55. Wang, D., Wu, H., Zhou, J., Xu, P., Wang, C., Shi, R., Wang, H., Wang, H., Guo, Z., and Chen, Q. (2018). In situ one-pot synthesis of MOF-polydopamine hybrid nanogels with enhanced photothermal effect for targeted cancer therapy. Adv. Sci. *5*, 1800287. https://doi.org/10.1002/advs.201800287.

56. Mi, Z., Yang, P., Wang, R., Unruangsri, J., Yang, W., Wang, C., and Guo, J. (2019). Stable radical cation-containing covalent organic frameworks exhibiting remarkable structure-enhanced photothermal conversion. J. Am. Chem. Soc. *141*, 14433–14442. https://doi.org/10.1021/jacs.9b07695.

STAR★METHODS

KEY RESOURCES TABLE

REAGENT or RESOURCE	SOURCE	IDENTIFIER
Antibodies		
Rabbit anti-Bcl-2	ABCAM	ab182858
Rabbit anti-Bax	ABCAM	ab32503
Mouse anti-caspase-3	ABCAM	ab145046
TNF-α	YEASEN	90621ES08
IL-1β	YEASEN	90165ES10
IL-10	YEASEN	90109ES10
Experimental models: Organisms/strains		
Female nude mice	Changzhou Cavens	SCXK2021-0013
Experimental models: Cell lines		
HepG2	Beyotime	C6346
HCCLM3	Beyotime	C6303
MHCC-97H	Beyotime	C6585
Chemicals and recombinant proteins		
3,3′-dithiol-4,4′-diamino-biphenyldiamine,4,4′,4′′, 4′′′′-(ethene-1,1,2,2-tetrayl) tetrabenzaldehyde	Aladdin	B399346
RuCl [(R,R)-TsDPEN] (mesitylene)	Aladdin	C-282761
Acetic acid (CH_3CO_2H)	Aladdin	A433221
Tetrahydrofuran (C_4H_8O)	Aladdin	T431413
Dichloromethane (CH_2Cl_2)	Aladdin	D116143
1,4-dioxane ($C_4H_8O_2$)	Aladdin	D166158
Silver nitrate ($AgNO_3$)	Aladdin	S433968
$Pt(NH_3)_2Cl_2$	Aladdin	C295225
Sodium hydroxide (NaOH)	Aladdin	S111502
Critical commercial assays		
Apoptosis Detection Kit	Beyotime	C1052
DiI (red fluorescent probe for cell membrane)	Beyotime	C1036
Annexin V-FITC/PI apoptosis detection kit	Beyotime	C1065M
Calcein-AM and PI staining analysis Kit	Beyotime	BB-4101
Deposited data		
Raw data	This paper	N/A
Software and algorithms		
GraphPad Prism	GraphPad	Prism 9
FlowJo	FlowJo	FlowJo 10
Other		
TEM	Thermo Fisher	Talos L120C G2
SEM	CarlZeiss	Gemini SEM 300
DLS analyzer	Malvern Panalytical	Zetasizer Nano ZS90
UV-vis spectrophotometer	Mapada	UV-1800(PC)
FT-IR	HORIBA	FluoroMax-4
FACScelesta	FAC	SAria II

RESOURCE AVAILABILITY

Lead contact

Further information and requests for resources should be directed to and will be fulfilled by the lead contact, Guiyang Zhang (guiyangzhang@ahmu.edu.cn).

Materials availability

New unique reagents were not produced in this work.

Data and code availability

- Data reported in this paper will be shared by the lead contact upon request.
- This paper does not report original code.
- Any additional information required to reanalyze the data reported in this work paper is available from the lead contact upon request.

EXPERIMENTAL MODEL AND SUBJECT DETAILS

Animals and tumor models

Female nude mice (5 weeks old, 16 to 18 g) were provided by Changzhou Cavens Laboratory Animal Co., Ltd (Jiangsu, China) and held under specific pathogen-free conditions. To build a tumor model, HepG2/HCCLM3/MHCC-97H cells (5×10^6 cells in 100 μL of complete culture medium) were injected into the right axillary of mice. When the tumor size approached 100 mm^3, experiments were performed. All mice were raised according to the guidelines approved by the Animal Protection Committee of Anhui Medical University. All animal care and handling procedures were performed in accordance with the National Institutes of Health's Guide for the Care and Use of Experimental Animals, and approved by the Animal Ethics Committee of the authors' institution (No. 14–862).

Cell culture

HepG2/HCCLM3/MHCC-97H cells were used as the research object in cell culture. Cells were cultured in DMEM containing fetal bovine serum (v/v = 10%), penicillin (100 U/mL) and streptomycin (0.1 mg/mL) at 37°C in a 5% CO_2 cell incubator. HepG2/HCCLM3/MHCC-97H cells were subcultured by the pancreatic enzyme/EDTA method. Cells were used for the experiment in the logarithmic growth phase. These cells were confirmed to be mycoplasma-free (last tested in 2022).

METHOD DETAILS

Synthesis of AIEgen-based COF (TPE-s COF)

A 10-mL Pyrex tube was charged with 4,4′,4′′,4′′′-(ethene-1,1,2,2-tetrayl) tetrabenzaldehyde (5 mg, 0.00984 mmol), 2.8 mg 3,3′- dithiol-4,4′-diamino-biphenyl (0.0197 mmol), and dioxane/mesitylene (4 mL, 1/1 by vol.). The mixture was sonicated for 30 sec, degassed through three freeze–pump–thaw cycles, sealed under vacuum, and heated at 120°C for 3 days and additional days at 90°C. The reaction mixture was cooled to room temperature and the light-yellow precipitate was collected by centrifugation. The precipitate was washed with anhydrous THF several times, further washed with anhydrous acetone, centrifuged, and dried under vacuum at room temperature for 24 h to yield light yellow powder. The sample was dispersed in anhydrous acetone and used for FE SEM and fluorescence microscope samplings.

Synthesis of TPE-s COF-Au

0.05 mL of 10 mM $HAuCl_4$ solution was added dropwise to 1 mL of TPE-s COF dispersion and dispersed by stirring. Then, 0.5M NaOH solution was added with slow stirring to adjust the pH to 12. Finally, $NaBH_4$ was slowly added dropwise to change the solution from initial yellow to reddish-brown and finally to light black. The product was purified by (3000Da) dialysis.

Synthesis of TPE-s COF-Au@Cisplatin

First, 2 mg of TPE-s COF-Au was dispersed in 1 mL of 1,4-dioxane by stirring and maintained at a pre-determined temperature of 37°C with a water bath for 20 min. Afterward, 4 mg of Cisplatin was dissolved in 2 mL of water and the aqueous solution was slowly added within 2 h, followed by the injection of 7 mL of water within 1 h. After the stirring for another 2 h, 1, 4-dioxane and the free Cisplatin were removed by dialysis

(MWCO 1 kDa) against deionized water. The TPE-s COF-Au@ Cisplatin carrier was obtained after freeze-drying. The drug loading capacity (DLC) of the obtained carriers was then analyzed by a UV absorption spectroscopy according to the following formula: Drug loading capacity = mass of drug in NP/mass of NP × 100%.

Synthesis of M@TPE-s COF-Au@ cisplatin

HepG2 cells were suspended in a cell culture medium (cell density 1×10^6–1×10^7/mL), then an appropriate amount of freeze-dried product TPE-s COF-Au@ Cisplatin was added for co-culture for 6 h. After centrifugation and resuspension, the cells were placed in an uncontrolled-rate cell cryopreservation medium, and the cell culture medium was soaked in liquid nitrogen for 12 h. Before use, the culture medium was thawed at 37°C and the shock cells were centrifuged in liquid nitrogen for 3 min. After being washed with PBS solution at pH 7.4, the shock cells were suspended in PBS and kept at 4°C.

Preparation of shock cells

HepG2 cells were centrifuged for 3 min and suspended in the uncontrolled cell cryopreservation solution with a cell density of 1 × 106 × 10^7 mL^{-1}, and the cell culture solution was soaked in liquid nitrogen for 12 h. Before use, the culture medium was thawed at 37°C and the shock cells were centrifuged for another 3 min. After the shock cells were washed with PBS solution, they were suspended in PBS and kept at 4°C.

Cell uptake analysis

For the cellular uptake study, DiI (red fluorescent probe for cell membrane) was used in this study. To qualitatively observe cell uptake, cells were first cultured on a 14 mm slide for 24 h, and then a TPE-s COF-Au sample was added to interact with the cells. After 4 h, the cells were washed with PBS, and the PBS was aspirated. Then 100 μL of DiI staining working solution was added to the corner of the slide and gently shook to cover all cells evenly with the dye. After incubating the cells at 37°C for 20 min, the working solution for staining was aspirated. Then all cells were covered with a pre-warmed culture medium and the slides were washed 2–3 times (5–10 min for each incubation), and then the culture medium was dried. The cells were then observed with a confocal laser scanning microscopy (CLSM) (excitation wavelength: 405 nm, emission wavelength: 440–470 nm; DiI, excitation wavelength: 550 nm, emission wavelength: 567 nm).

Cytotoxic studies of different materials

Cytotoxicity studies are critical for evaluating the biocompatibility, safety, and therapeutic efficacy of the resulting materials. In this work, the toxicity of materials to cells was detected by the MTT method, Annexin V-FITC/PI apoptosis detection method, and Calcein-AM/PI staining method.

MTT experiment

First, HepG2 cells (5×10^3/well) were cultured on 96-cell culture plates for 24 h. The cytotoxicity was determined after incubating different concentrations of Cisplatin, laser, TPE-s COF-Au, TPE-s COF-Au@ Cisplatin, TPE-s COF-Au@ Cisplatin + laser, M@TPE-s COF-Au@ Cisplatin + laser (concentration range: 12.5–200 μg/mL) with HepG2 cells at 37°C for 48 h, respectively. After endocytosis for 48 h, cells were washed with fresh complete culture solution and then irradiated with or without 808 nm laser (1.0 W/cm^2, 5 min). Cell viability was detected with the standard MTT method and was further analyzed. The absorbance at 450 nm was detected with a microplate reader. Cell viability was calculated by the formula: Cell viability = (OD Experimental group – OD Blank)/(OD Control -OD Blank) ×100%.

Annexin V-FITC apoptosis detection experiment

The apoptosis of cells in each experimental group was detected on BD FACScelesta, and the cells were stained with Annexin V-FITC/PI apoptosis detection kit (YEASEN, Shanghai). First, HepG2 cells were seeded in a 6-well cell culture plate with a cell density of 1×10^5/well. After 24 h of culture, the cells were incubated for 24 h with the complete culture solution containing PBS, Cisplatin, laser, TPE-s COF-Au, TPE-s COF-Au@ Cisplatin, TPE-s COF-Au@ Cisplatin + laser, M@TPE-s COF-Au@ Cisplatin + laser (200 μg/mL). After being washed with a fresh complete culture medium, the cells were irradiated with or without 808 nm laser (1.0 W/cm^2, 5 min) and then incubated for 6 h in the dark. Then the cells were collected and stained with Annexin V-FITC (5 μL) and PI (10 μL) for 20 min in the dark. The stained cells were analyzed by flow cytometry (FC) and the recorded data were statistically analyzed with FlowJo 10.0 software.

Calcein-AM and PI staining analysis experiments

After HepG2 cells interacted with the material and were stained with Calcein-AM and PI, their situation (live/dead) visible to naked eyes was observed under a fluorescence microscope. Briefly, cells (1×10^4/well) were placed in a 6-well culture plate for 24 h, then treated with 200 μg/mL of material and incubated continuously for 8 h. After being washed, the cells were replaced with fresh culture solution, which was laser irradiated or not irradiated, respectively. After a 12-h incubation in the dark, the cells were stained with Calcein-AM (2.0 μM) and PI (1.5 μM) at 37°C for 15 min. Finally, after the wash with PBS, the cells were imaged under a fluorescence microscope.

Animal and tumor models

Female nude mice (5 weeks old, 16 to 18 g) were provided by Changzhou Cavens Laboratory Animal Co., Ltd. To build a tumor model, HepG2/HCCLM3/MHCC-97H cells (5×10^6 cells in 100 μL of complete culture medium) were injected into the right axillary of mice. When the tumor size approached 100 mm^3, experiments were performed.

In vivo and *in vitro* fluorescence imaging

To observe the targeting effect of the prepared TPE-s COF-Au@ Cisplatin and M@TPE-s COF-Au@ Cisplatin materials in real time, the American Spectral Instrument small animal imaging system was used to observe and image the NIR fluorescence of the materials and mice at different time points. The parameters were set as follows: excitation wavelength 430 nm, emission wavelength 510 nm, and exposure time 30 s. Then, 1 mL of TPE-s COF-Au@ Cisplatin and M@TPE-s COF-Au@ Cisplatin dispersions (200 μg/mL) were placed into 1.5 mL EP tubes to observe the fluorescence characteristics of the dispersions. Subsequently, 200 μL of TPE-s COF-Au@ Cisplatin and M@TPE-s COF-Au@ Cisplatin (at a Cisplatin concentration of 1.5 mg/kg) were injected into tumor-bearing mice. Then, real-time fluorescence images of tumors were recorded within 2 to 96 h. In addition, the mice of TPE-s COF-Au@ Cisplatin and M@TPE-s COF-Au@ Cisplatin material groups were sacrificed after 72 h, and tissues such as heart, liver, spleen, lungs, kidneys, and tumors were taken for imaging. The fluorescence intensity of each tissue was recorded with Bruker molecular imaging software.

Synergistic therapy *in vivo*

Tumor-bearing mice were randomly divided into the following treatment groups (n = 6): PBS; Cisplatin, laser, TPE-s COF-Au, TPE-s COF-Au@ Cisplatin, TPE-s COF-Au@ Cisplatin + laser, M@TPE-s COF-Au@ Cisplatin + laser. According to different groups, tumor-bearing mice were given intravenously with 200 μL (1.5 mg/kg of Cisplatin concentration), with or without irradiation of 808 nm laser (1.0 W/cm^2, 5 min). Dosing and laser irradiation were performed every three days. During this process, the body weight and tumor size of the mice were tracked and recorded. At the same time, temperature fluctuations at the tumor site and infrared images of mice were recorded with an infrared thermal imaging camera. Tumor sizes from different experimental groups were measured with calipers every 3 days. After 27 days of the experiment, the main organs and tumor tissues of the mice in the PBS and material groups were collected. Major organs were stained with hematoxylin-eosin (H&E). Tumor tissues were stained with H&E staining, γ-H2AX terminal deoxynucleotide transferase dUTP nick end labeling (TUNEL) and immuno-histochemical staining of Ki-67, Bcl-2, caspase-3 and Bax.

QUANTIFICATION AND STATISTICAL ANALYSIS

The results were expressed as mean ± standard deviation (mean ± SD). The Student's *t* test was used for comparison between two groups, and one-way analysis of variance (ANOVA) was used for the comparison among three or more groups. The survival curve was tested using the log rank (Mantel-Cox) test. All statistical analyses were performed by GraphPad Prism 9 software (GraphPad, USA). Statistical significance is indicated as: $*p < 5 \times 10^{-2}$, $**p < 1 \times 10^{-2}$, and $***p < 1 \times 10^{-3}$.